

Assessment of high-resolution methods for numerical simulations of compressible turbulence with shock waves

Eric Johnsen^{a,*,1}, Johan Larsson^{a,*,1}, Ankit V. Bhagatwala^b, William H. Cabot^c, Parviz Moin^a, Britton J. Olson^b, Pradeep S. Rawat^d, Santhosh K. Shankar^b, Björn Sjögren^c, H.C. Yee^e, Xiaolin Zhong^d, Sanjiva K. Lele^b

^a Center for Turbulence Research, Stanford University, Stanford, CA 94305, United States

^b Department of Aeronautics and Astronautics, Stanford University, Stanford, CA 94305, United States

^c Lawrence Livermore National Laboratory, Livermore, CA 94551, United States

^d Department of Mechanical and Aerospace Engineering, University of California, Los Angeles, CA 90095, United States

^e NASA Ames Research Center, Moffett Field, CA 94035, United States

ARTICLE INFO

Article history:

Received 25 March 2009

Received in revised form 2 October 2009

Accepted 15 October 2009

Available online 21 October 2009

PACS:

47.11.–j

47.27.–e

Keywords:

Compressible turbulence

Direct numerical simulation

Large-eddy simulation

High-resolution methods

Shock-capturing

Hybrid methods

Artificial diffusivity methods

Adaptive characteristic-based filters

Shock fitting

ABSTRACT

Flows in which shock waves and turbulence are present and interact dynamically occur in a wide range of applications, including inertial confinement fusion, supernovae explosion, and scramjet propulsion. Accurate simulations of such problems are challenging because of the contradictory requirements of numerical methods used to simulate turbulence, which must minimize any numerical dissipation that would otherwise overwhelm the small scales, and shock-capturing schemes, which introduce numerical dissipation to stabilize the solution. The objective of the present work is to evaluate the performance of several numerical methods capable of simultaneously handling turbulence and shock waves. A comprehensive range of high-resolution methods (WENO, hybrid WENO/central difference, artificial diffusivity, adaptive characteristic-based filter, and shock fitting) and suite of test cases (Taylor–Green vortex, Shu–Osher problem, shock-vorticity/entropy wave interaction, Noh problem, compressible isotropic turbulence) relevant to problems with shocks and turbulence are considered. The results indicate that the WENO methods provide sharp shock profiles, but overwhelm the physical dissipation. The hybrid method is minimally dissipative and leads to sharp shocks and well-resolved broadband turbulence, but relies on an appropriate shock sensor. Artificial diffusivity methods in which the artificial bulk viscosity is based on the magnitude of the strain-rate tensor resolve vortical structures well but damp dilatational modes in compressible turbulence; dilatation-based artificial bulk viscosity methods significantly improve this behavior. For well-defined shocks, the shock fitting approach yields good results.

© 2009 Elsevier Inc. All rights reserved.

1. Introduction

Turbulence is a ubiquitous phenomenon in most fluid flows of scientific and engineering interest and significantly affects processes such as mixing, flow separation and combustion. Because of the complexity of turbulence, analytical solutions do not exist. However, numerical solutions to the Navier–Stokes equations in which all the dynamical scales in the flow field are resolved can be produced in certain cases; this approach is termed direct numerical simulation (DNS). In many practical applications, a resolution sufficient for DNS is not achievable, so that the viscous dissipation at the small scales is instead

* Corresponding authors. Tel.: +1 650 723 9286.

E-mail addresses: johnsen@stanford.edu (E. Johnsen), jola@stanford.edu (J. Larsson).

¹ These authors equally contributed to this work.

modeled; this approach is termed large-eddy simulation (LES). While many numerical methods rely on numerical dissipation for stability purposes, this unphysical dissipation reduces the range of well-resolved length scales in LES and DNS. Hence numerical dissipation has adverse effects on both accuracy and computational cost, particularly in LES, which is by definition under-resolved, but also in DNS. Since the present study is aimed toward LES, in which solutions are by definition under-resolved, poorly resolved solutions are considered.

Flows in which shock waves and turbulence are present and interact dynamically occur in a wide range of applications, e.g., inertial confinement fusion, supernovae explosion and scramjet propulsion. The main computational challenge of predicting compressible turbulence in general, and interactions between shock waves and turbulent flows in particular, arises from the contradictory properties of numerical methods designed to treat shocks and turbulence. Shock waves are extremely thin regions of widths on the order of a few mean free paths; in the context of the present work, they are considered to be sharp discontinuities, i.e., no attempt is made to resolve the physical shock structure. In order to represent shock waves in an accurate and stable fashion on a computational grid, most numerical schemes rely strongly on numerical dissipation [28,45], which results in smearing the shock over a few grid points. Such techniques are termed *shock-capturing*, as opposed to *shock tracking* or *shock fitting*, in which the shock position, shape and velocity are explicitly determined. The major drawback of using shock-capturing schemes in smooth turbulent regions is that the numerical dissipation invariably overwhelms the physical dissipation, which is precisely what numerical methods for turbulence simulations seek to avoid.

As illustrated by the broad range of algorithms in the literature, a number of different strategies have been used to overcome the difficulties of simultaneously treating shocks and turbulence. Certain methods employ purely shock-capturing finite difference approximations, e.g., based on the weighted essentially non-oscillatory (WENO) schemes of Jiang and Shu [21], possibly with improved wavenumber properties [10,33]. Other methods use characteristic-based filters in conjunction with artificial compression and wavelets as flow sensors to control the numerical dissipation [48,41]. A compact scheme may be employed with adaptive Padé-type filters to stabilize the solution near shocks [14,46]. Another avenue is the hybrid approach, in which a shock detector restricts the use of shock-capturing to regions near shocks in order to contain the dissipation in smooth regions [1,35]. Yet another approach consists of regularizing the governing equations by introducing numerical dissipation, e.g., artificial diffusivity [7,6,13,32] or hyper-diffusivity [20], and of solving the resulting system with high-order accurate methods. An alternative philosophy is to use shock fitting with an upwind scheme for problems with a single well-defined shock [52].

Analyzing the aforementioned methods theoretically is a challenging task due to their complexity; such methods are typically verified using different test problems and validated against experiments. However, it is difficult to establish a hierarchy based on the published work or even determine which method is the most appropriate for a given compressible turbulence problem because of the lack of comparisons between such schemes. At the present time, comparisons are restricted to a narrow class of methods and problems, e.g., shock-capturing schemes for shock-dominated flows [29,16]; artificial diffusivity methods for shocks [7,13,22] or purely broadband problems [8,6]; and monotone integrated LES or MILES [17], subgrid-scale modeling for LES [24] and the evaluation of shock-capturing schemes in LES [15] for compressible turbulence.

The objective of the present study is to provide an evaluation of a suite of numerical methods that can and have been used to simulate problems in which shocks and turbulence are both present and interact dynamically. The key aspect of this work is the comprehensive range of methods and suite of relevant test problems that are considered to best evaluate the strengths and weaknesses of the current algorithms. Several high-resolution algorithms (WENO, hybrid WENO/central difference, artificial diffusivity, adaptive characteristic-based filter and shock fitting) are considered. Problems with purely smooth and broadband features (Taylor–Green vortex) and well-defined discontinuities (Shu–Osher problem, shock-vorticity/entropy wave interaction, Noh problem) are chosen, along with, more importantly, a combination thereof (compressible isotropic turbulence with eddy shocklets); the latter problem turns out to be surprisingly discriminating. Under-resolved results are presented to illustrate the effects of numerical dissipation on a fixed (coarse) grid; the assessment of the numerical methods considered in the present work may differ when considering the fully resolved case. The article is organized as follows. First, a brief description of the numerical framework is included in Section 2. The test problems used to evaluate the different methods are then described in Section 3 and the results from each method are presented. Section 4 contains discussions of more general nature, not directly linked to any specific test case. Finally, the article ends with some concluding remarks and an outlook for future work. The results for each algorithm were computed by the individual code developers, and the findings reported in the present article are the result of a collaborative project under DOE-SciDAC sponsorship.

2. Numerical framework

2.1. Governing equations

The compressible Navier–Stokes equations for a calorically perfect gas are solved:

$$\frac{\partial \rho}{\partial t} + \nabla \cdot (\rho \mathbf{u}) = 0, \quad (1a)$$

$$\frac{\partial (\rho \mathbf{u})}{\partial t} + \nabla \cdot (\rho \mathbf{u} \mathbf{u} + p \delta) = \nabla \cdot \tau, \quad (1b)$$

$$\frac{\partial E}{\partial t} + \nabla \cdot (\mathbf{u}(E + p)) = \nabla \cdot (\mathbf{u} \cdot \tau - \mathbf{q}), \quad (1c)$$

where ρ is the density, \mathbf{u} is the velocity vector, p is the pressure, δ is the unit tensor, $E = \rho e + \rho \mathbf{u} \cdot \mathbf{u}/2$ is the total energy, e is the specific internal energy, τ is the viscous stress tensor, and \mathbf{q} is the heat flux. Setting the right-hand side of Eq. (1) to zero reduces the system to the Euler equations. The following equation of state is used:

$$p = (\gamma - 1)\rho e, \quad (2)$$

where γ is the ratio of specific heats. The viscous stress tensor is defined as

$$\tau = 2\mu_s \mathbf{S} + \left(\mu_b - \frac{2}{3}\mu_s\right)(\nabla \cdot \mathbf{u})\delta, \quad (3)$$

where $\mathbf{S} = (\nabla \mathbf{u} + (\nabla \mathbf{u})^T)/2$ is the strain-rate tensor, μ_s is the dynamic shear viscosity and μ_b is the bulk viscosity; the viscosities are related via Stokes' hypothesis. The heat flux is defined as

$$\mathbf{q} = -k\nabla T, \quad (4)$$

where k is the thermal conductivity, $T = (\gamma - 1)e/R$ is the temperature, and R is the gas constant.

2.2. Numerical methods

The first key aspect of the present work is the comprehensive nature of the evaluated numerical methods. Six high-resolution and high-order accurate methods based on different approaches to computing shock waves and turbulence are considered. Though third-order accuracy in space is typically considered high-order accurate in the literature, the present schemes are at least fifth- and up to 10th-order accurate in smooth regions. The methods are briefly described below, with more detailed descriptions provided in [Appendix B](#). All problems are solved on uniform Cartesian grids.

2.2.1. Artificial diffusivity methods

The guiding philosophy behind artificial diffusivity methods is to first regularize the equations through the addition of diffusive terms based on artificial properties, and then to solve the regularized equations using a high-order accurate scheme. A key property is the discrimination between vortical and dilatational structures through the shear and bulk viscosities, respectively. The amount of artificial shear and bulk viscosity, thermal conductivity and mass diffusivity is controlled by tunable coefficients, for which a fixed set of values is used in this study.

In the present work, a sixth-order accurate compact finite difference scheme optimized for high-wavenumber resolution is employed to compute the spatial derivatives [30]. The convective term of the momentum equation is written in skew-symmetric form² and the viscous terms in the momentum and energy equations are computed in non-conservative form. An eleven-stage Runge–Kutta scheme optimized for low dispersion errors is employed [19,43]. At every Runge–Kutta substep, an eighth-order accurate filter is applied to the conservative variables to remove aliasing errors.

One of the key findings of the present collaborative work is that the artificial bulk viscosity proposed by Cook [6] causes excessive damping of dilatational and thermodynamic fluctuations in compressible turbulence; this drawback is discussed in the next section and was also noted in Ref. [9]. This finding prompted Mani et al. [32] to define the artificial bulk viscosity in terms of the dilatation (rather than the strain-rate tensor), to prevent excessive damping of the dilatational motions. The key improvement stems from the realization that dilatation and the magnitude of the strain-rate tensor are similar at a shock, but that the former is orders of magnitude smaller in turbulence. In follow-up work, Bhagatwala and Lele [3] used the insight from [32] to define a slightly different artificial bulk viscosity. In order to illustrate the recent progress on artificial diffusivity methods, results from two methods using different models for the artificial bulk diffusivity but with the same underlying numerics are used in the present study:

1. *Stan*: the original model of Cook [6].
2. *Stan-I*: the improved model of Bhagatwala and Lele [3].

A discussion of artificial diffusivity methods is provided in [Appendix C](#), in order to clarify the differences and drawbacks/advantages of the different models proposed over the past few years.

2.2.2. Hybrid WENO/central difference method

The code labeled *Hybrid* [26] is based on the principle that turbulence and shock waves are fundamentally different phenomena and should thus be treated differently. Hence, to distinguish shock waves from smooth turbulent regions, the *Hybrid* method relies on a shock sensor based on vorticity and dilatation that is similar to that of Ducros et al. [11]. In smooth regions, a sixth-order accurate central differencing scheme is applied in split (or 'skew-symmetric') form for improved nonlinear stability [12]. In discontinuous regions, a fifth-order accurate WENO scheme is used. The hybrid nature of the code creates internal interfaces between the central and WENO regions, the stability of which was analyzed in Ref. [25]. The *Hybrid* code uses a fixed set of coefficients for all the test problems, except that the shock sensor in the Shu–Osher problem is

² The term 'skew-symmetric' is used here, although it strictly only applies to the limit of incompressible flow; for compressible flow, the 'skew-symmetric' form of the convective term does not satisfy the mathematical definition of a skew-symmetric operator.

that of Hill and Pullin [18], because this problem is one-dimensional. The time-marching is handled using a standard fourth-order accurate Runge–Kutta scheme.

2.2.3. WENO method

The WENO code consists of a seventh-order accurate conservative finite difference WENO scheme for the interpolation, Roe flux-splitting with entropy fix for the upwinding [21], and a carbuncle fix [37]. The time-marching is handled using a standard fourth-order accurate Runge–Kutta scheme.

2.2.4. Adaptive characteristic-based filter method

ADPDIS3D is a three-dimensional variable high-order accurate multiblock overlapping grid code in curvilinear geometries. It includes a unified treatment of gas dynamics/MHD (magnetohydrodynamics), multifluid, combustion and nonequilibrium flows. The code is based on low-dissipation high-order accurate filter methods in finite difference formulation [48,41,50,51]. Such a filter method consists of two steps: a full time step using a spatially high-order non-dissipative base scheme, followed by a post-processing filter step. The post-processing filter step consists of the products of wavelet-based flow sensors and linear and nonlinear numerical dissipations. The flow sensor is used in an adaptive procedure to analyze the computed flow data and indicate the amount, location and type of built-in numerical dissipation that can be eliminated or further reduced. Unlike standard shock-capturing and/or hybrid shock-capturing methods, the nonlinear filter method requires one Riemann solve per dimension, independent of time discretizations. Conservative and non-conservative skew-symmetric splitting of the gas dynamics equations [49,42] are included in the code.

In all of the present test cases, the base scheme consists of eighth-order accurate central differencing, and a nonlinear filter is used. At the completion of the full time step of the fourth-order Runge–Kutta temporal discretization, the computed solution is filtered by the dissipative portion of a seventh-order accurate WENO scheme using the Roe flux with a three-level second-order wavelet decomposition of the computed data as the flow sensor. The flow sensor monitors the density and pressure computed data. A single block grid is used for all computations. The conservative skew-symmetric splitting [42] of the governing equation are employed for all test cases except for the Noh problem. This is due to the fact that employing higher than sixth-order base scheme and fifth-order shock-capturing filter in conjunction with the skew-symmetric splitting form is not stable for this test case. When the un-split form of the convective terms in Eq. (1) and a 10th-order linear dissipation are used for the base scheme step in conjunction with the seventh-order WENO filter, a stable solution can be obtained.

2.2.5. Shock-fitting method

The code labeled *Shock Fit* is based on the shock-fitting method of Zhong [52], which treats the shock as a sharp entity and solves the compressible Navier–Stokes equations in conservation form in the computational domain. The shock velocity and the flow variables behind the shock are obtained using the Rankine–Hugoniot relations coupled with a characteristic compatibility equation. The location and geometry of the shock is modified according to the shock velocity and shock-fitted curvilinear grids are used. In the shock fitting approach, any scheme can be used to solve the governing equations in the computational domain. In the present calculations, a fifth-order accurate upwind finite difference scheme [52] is used to discretize the governing equations. The time marching is handled using a third-order accurate Runge–Kutta scheme.

Results are shown only for problems with initially well-defined shocks (Shu–Osher problem and shock-vorticity/entropy wave interaction), with a fixed set of coefficients.

2.3. Estimates of the computational cost

In the present work, the different discretizations, options and capabilities of each code, which may vary depending on the problem, make it difficult to conduct a fair comparison. A quantitative estimate of the performance of each code can be made by counting the number of floating point operations required to compute the convective terms, as shown in Table 1. All the codes are based on finite differences and use similar time marching (except for the *Stan* codes). Differences in the computational cost therefore mainly reside in the spatial discretization. The code descriptions in Appendix B provide the required information to count the number of operations; the numbers given in Table 1 are estimates, as the effective implementation of the algorithms is expected to vary from one programmer to the next. The estimates for the central differences are for the split form of the convective terms; also, local Lax–Friedrichs flux-splitting is considered for the WENO scheme in this section only to avoid issues related to logical statements in the upwinding. The large difference in operations between fifth- and seventh-order accurate WENO comes from the calculation of the smoothness indicators.

The *Hybrid* code cannot be assessed as such, since the fraction of points treated by WENO depends on the solution. We therefore give estimates for the pure central (sixth-order accurate) and WENO (fifth-order accurate) components of this method; in many problems of interest, the fraction of points computed using WENO is expected to be small, so that the cost of the WENO scheme is small, and the real impact of the WENO scheme in the *Hybrid* code is to make parallel load-balancing non-trivial. The ADPDIS3D code employs a central base scheme at every Runge–Kutta substep. The computed solution is then filtered by a post-processing step using the dissipative portion of a seventh-order WENO scheme after each full time step. Although ADPDIS3D should compute the WENO filter step only at grid points indicated by the wavelet flow sensor, for parallel implementation, it is easier to compute the filter step at every grid point. The artificial diffusivities in the *Stan* code

Table 1

Estimated number of operations required to compute the convective terms per grid point per Runge–Kutta substep. The order of accuracy of the central difference and WENO schemes are included in parentheses. For the *Stan* codes, the 11 Runge–Kutta evaluations march the solution forward by two time steps. For the *ADPDIS3D* code, the spatial central base scheme is employed at every Runge–Kutta substep, but the WENO filter step is only employed after the completion of the full time step.

Code	# RK eval.	# Derivative eval. (1st and 2nd)	# Ops/grid point
<i>Stan</i>	11/2	24 and 42	1900
<i>Stan-I</i>	11/2	24 and 42	1900
Central difference (6)	4	33 and 0	1100
Central difference (8)	4	33 and 0	1600
WENO (5)	4	15 and 0	3100
WENO (7)	4	15 and 0	6200

imply that the diffusive terms must be evaluated even for inviscid problems; for fairness, the estimates in the table only include the calculation of the artificial diffusivity coefficients, but not the computation of the derivatives.

The cost of computing the viscous terms is non-trivial. The number of operations depends on how these terms are evaluated (conservative vs. non-conservative form) and on the numerics. When computing these terms in conservative form, 24 first derivatives must be evaluated; when computing these terms in non-conservative form, 27 (or 34 for artificial diffusivity methods) first derivatives must be evaluated. For instance, using the sixth-order accurate central difference scheme in the *Hybrid* code, approximately 300 operations are needed for the conservative evaluation, and an additional 50 operations are required for the non-conservative form; using the present compact scheme in the *Stan* code, almost 700 operations are needed for the conservative evaluation, and an additional 350 are required for the non-conservative form.

We finally note that the parallel efficiencies of the *Hybrid*, *WENO*, and *ADPDIS3D* methods are higher than those of the *Stan* and *Stan-I* ones, due to the need for matrix-inversions in the latter. In other words, the methods relying on matrix-inversions tend to spend more time on communication than the other methods.

3. Test problems

The second key element in the present work is the comprehensive suite of benchmark problems. Since the end applications of interest all share the common trait of simultaneously involving broadband turbulence and sharp discontinuities (shocks and contact surfaces), the test problems are chosen in an attempt to isolate one or more relevant properties and to eventually combine them. The problems are ordered in a sequence of increasing complexity (by some measure): first the shock-free but broadband three-dimensional Taylor–Green vortex; then a series of non-broadband shock problems (one-dimensional Shu–Osher problem, two dimensional shock-vorticity/entropy wave interaction), culminating in the infinite-strength three-dimensional Noh implosion; and a three-dimensional compressible isotropic turbulence problem with broadband spectra and eddy shocklets. The last problem is the only viscous problem. Two sets of results are presented: a converged solution and a solution on a coarse grid. Given the number of methods (and thus the number of lines in each plot), a consistent color and line scheme is used, as listed in Table 2. The reader is referred to the online version of this article for color figures.

3.1. Taylor–Green vortex

From a well-resolved initial condition, the inviscid Taylor–Green vortex [44] begins stretching and producing ever smaller scales. It thus constitutes a non-regularized problem with no lower bound on the length scale and is solved with no regularization other than that provided by the numerical method. The goal of this problem is to provide a test of the stability of the methods for severely under-resolved motions, as well as a measure of the preservation of kinetic energy and the growth of enstrophy.

The three-dimensional Euler equations are solved with gas constant $\gamma = 5/3$. The domain $x_i \in [0, 2\pi)$ is periodic and the grid spacing is $\Delta x_i = 2\pi/64$. The initial conditions are

Table 2

Color and line legend for the plots. The reader is referred to the online version of this article for color figures.

Code	Color	Line style
Reference	Black	varying
<i>Stan</i>	Red	Dashed
<i>Stan-I</i>	Magenta	Dashed (thin)
<i>Hybrid</i>	Blue	Solid
WENO	Cyan	Solid (thin)
ADPDIS3D	Green	Dashed-dotted
Shock Fit	Black	Dotted

$$\rho = 1, \quad (5a)$$

$$u_1 = \sin x_1 \cos x_2 \cos x_3, \quad (5b)$$

$$u_2 = -\cos x_1 \sin x_2 \cos x_3, \quad (5c)$$

$$u_3 = 0, \quad (5d)$$

$$p = 100 + \frac{[\cos(2x_3) + 2][\cos(2x_1) + \cos(2x_2)] - 2}{16}, \quad (5e)$$

where the mean pressure is sufficiently high to make the problem essentially incompressible. The numerical results are compared to the semi-analytical solution for the enstrophy growth by Brachet et al. [4] for $t \leq 4$, where $t \leq 3.5$ was considered well-converged. In the incompressible problem the kinetic energy should remain constant while the enstrophy grows rapidly.

Fig. 1 shows the temporal evolution of the mean kinetic energy, $\langle \rho u_i u_i \rangle / 2$, and enstrophy, $\langle \omega_i \omega_i \rangle / 2$, where $\omega = \nabla \times \mathbf{u}$ is the vorticity, normalized by their initial values. The brackets denote averaging over all space: for a function q ,

$$\langle q \rangle = \frac{1}{L^3} \int_0^L \int_0^L \int_0^L q(x_1, x_2, x_3) dx_1 dx_2 dx_3, \quad (6)$$

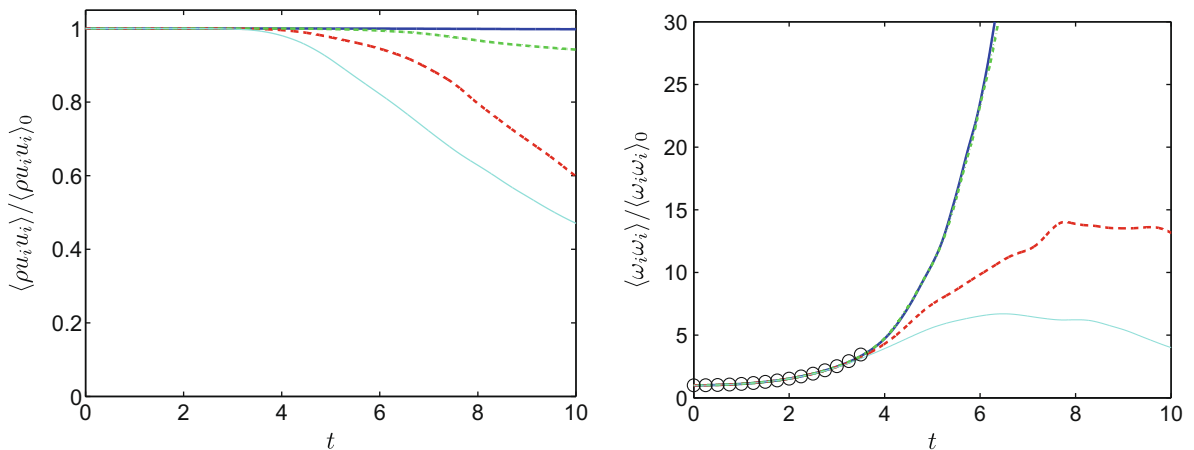
with the RMS value defined as $q_{\text{rms}} = \sqrt{\langle q^2 \rangle - \langle q \rangle^2}$.

The dilatation-based shock sensor in the *Hybrid* code never activates the WENO scheme for this problem, allowing the non-dissipative central scheme to preserve the kinetic energy. The *ADPDIS3D* code is essentially non-dissipative, with only a slight decrease toward the end of the simulation. These two methods also give the most rapid growth in enstrophy. The *WENO* code is the most dissipative of all the methods for this problem; it begins adapting its stencils at $t \approx 3$, which drastically increases the numerical dissipation, thus leading to underpredictions in the kinetic energy and enstrophy. The *Stan* code lies somewhere in between the *Hybrid*/*ADPDIS3D* and *WENO* results. Note that the improved *Stan-I* results are identical to those of *Stan* for this problem, since the solenoidal velocity field is insensitive to the bulk viscosity. On the present grid, all methods agree with the semi-analytical results for the enstrophy growth.

In order to provide a quantitative comparison of the codes, the mean kinetic energy normalized by its initial value is tabulated at $t = 5$; at this time, dissipation effects have become evident. Also, the mean enstrophy normalized by its initial value is tabulated at $t = 3.5$; this is the last time for which semi-analytical results are obtained. These two values are shown in Table 3 and exhibit a behavior similar to that plotted in Fig. 1. Such metrics provide quantitative means for other researchers to evaluate their codes against the present algorithms.

Next, the velocity spectra at $t = 5$ are shown in Fig. 2. No analytical spectrum is known at this time, so a converged reference solution is first determined. While the problem is unregularized with no lower bound on the length scale, one can argue that for a fixed time it is possible to converge the spectrum for a limited range of wavenumbers. The range of interest here is $k \leq 32$, given that 64^3 grids are employed. To generate a reference solution, the velocity spectrum is computed on a sequence of grids using the *Hybrid* code in both non-dissipative form and with the addition of an eighth-order accurate dissipation term, which effectively removes numerical noise. The results of this exercise are shown in Fig. 2a, where it is clear that the lower wavenumbers converge. Specifically, the range $k \leq 32$ is converged on the 256^3 grid.

Comparing to this reference, the minimally dissipative *Hybrid* and *ADPDIS3D* codes agree well for $k \leq 20$ and show energy pile-up past this point; this agrees with the expected onset of aliasing errors at $2/3$ of the maximum wavenumber,



(a) Kinetic energy.

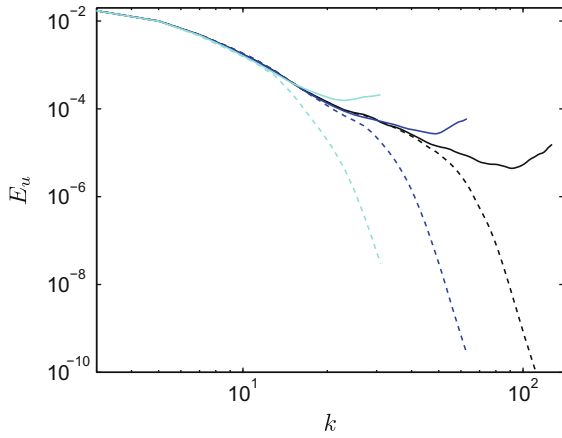
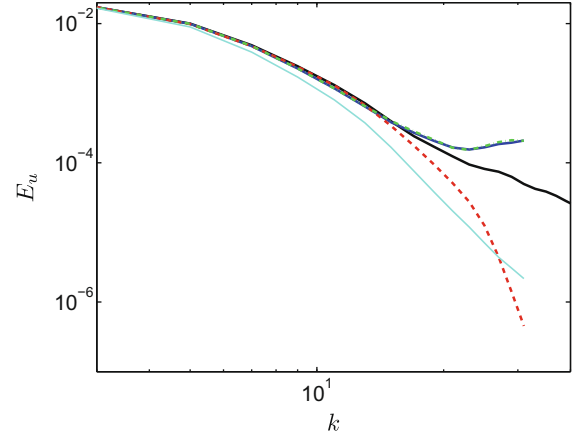
(b) Enstrophy. The semi-analytical result of Brachet et al. (1983) are the black symbols.

Fig. 1. Mean quantities for the Taylor–Green vortex on a 64^3 grid. The zero subscript denotes the initial value.

Table 3

Accuracy metrics for the Taylor–Green vortex, with the semi-analytical result of Brachet et al. [4].

	<i>Hybrid</i>	<i>ADPDIS3D</i>	<i>Stan</i>	<i>Stan-I</i>	<i>WENO</i>	Brachet et al. [4]
<i>T-G</i> energy $t = 5$	1.00	0.998	0.976	0.976	0.916	1.00
<i>T-G</i> enstrophy $t = 3.5$	3.33	3.34	3.23	3.23	3.13	3.46

(a) Convergence of the reference solution using the *Hybrid* code in standard mode (solid) and with eighth-order accurate dissipation (dashed) on 256^3 (black), 128^3 (blue), and 64^3 (cyan).(b) Comparison between the different schemes. The reference solution is that obtained on the 256^3 grid using the *Hybrid* code.**Fig. 2.** Velocity spectra for the Taylor–Green vortex on 64^3 grid at $t = 5$.

though nonlinear processes are expected to redistribute the energy. The *Hybrid* code eventually reaches an equi-partitioned spectrum. The stability in lieu of dissipation is solely due to the split form of the convective terms; in a conservative form, the code diverges after $t \approx 4$ (data not shown). The *Stan* codes agree with the reference for $k \lesssim 16$ and then underpredicts the spectrum, while the *WENO* code agrees only for $k \lesssim 8$ despite being formally high-order accurate. The dealiasing filter in the *Stan* code directly affects only the very highest wavenumbers. The damping for $k \gtrsim 16$ therefore implies either that the cumulative effect of the many filter operations decreases the effective bandwidth, or that nonlinear processes distribute the damping to lower wavenumbers.

3.2. Shu–Osher problem

The Shu–Osher problem [39] is a one-dimensional idealization of shock-turbulence interaction in which a shock propagates into a perturbed density field. The goal of this problem is to test the capability to accurately capture a shock wave, its interaction with an unsteady density field, and the waves propagating downstream of the shock.

The one-dimensional Euler equations with $\gamma = 1.4$ are solved on the domain $x \in [-5, 5]$ with $\Delta x = 0.05$ and initial conditions

$$(\rho, u, p) = \begin{cases} (3.857143, 2.629369, 10.33333), & x < -4, \\ (1 + 0.2 \sin(5x), 0, 1), & x \geq -4. \end{cases} \quad (7)$$

This problem corresponds to a $M = 3$ shock moving into a field with a small density (or entropy) disturbance. The solution is compared to a reference solution with $\Delta x = 6.25 \times 10^{-3}$.

Fig. 3 shows the density, Fig. 4 shows the entropy, and Fig. 5 shows the velocity, all at $t = 1.8$. The entropy is given by $\Delta s/c_v = \ln(p/\rho^\gamma)$, where c_v is the specific heat at constant volume. The interaction between the shock and the entropy disturbance generates both acoustic and entropy waves downstream of the shock. The acoustic waves are strong enough to steepen into weak shock waves. At the given time, the shock location is $x_s \approx 2.39$, the location of the contact discontinuity at the leading entropy wave is $x_c \approx 0.69$, and the location of the leading acoustic wave is $x_a \approx -2.75$. The initial entropy waves have wavelength $\lambda_1 = 2\pi/5$, which by conservation of mass in a frame moving with the main shock is approximately 0.33 in the post-shock region. For the present grid, the entropy waves behind the shock have 6.5 points per wavelength. All codes yield the correct shock location and capture the shock reasonably well.

Since the presence of both acoustic and entropy waves complicate the density plot, which is typically shown for this problem, entropy and velocity profiles are considered to isolate each family of waves. The most prominent difference between the

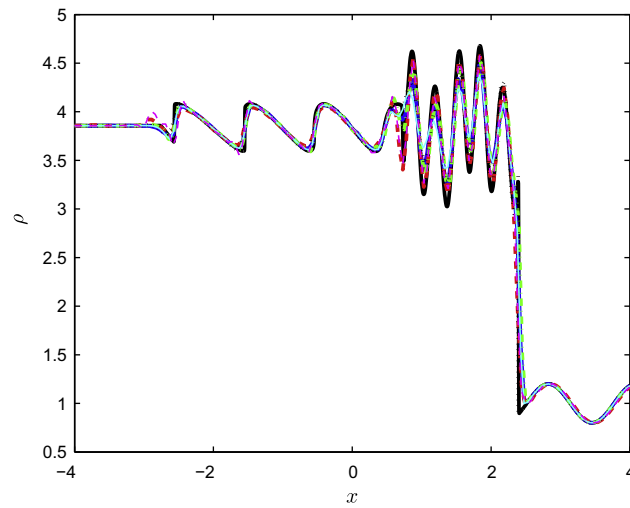
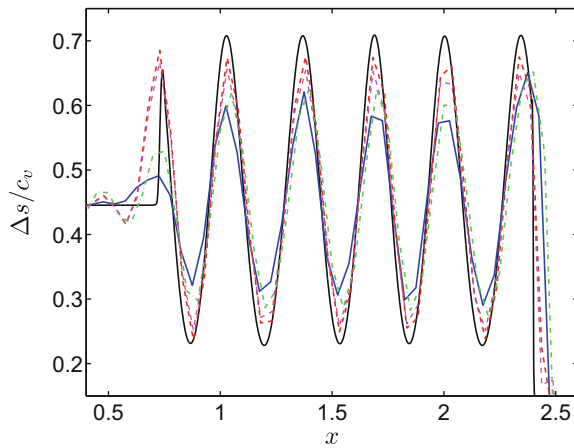
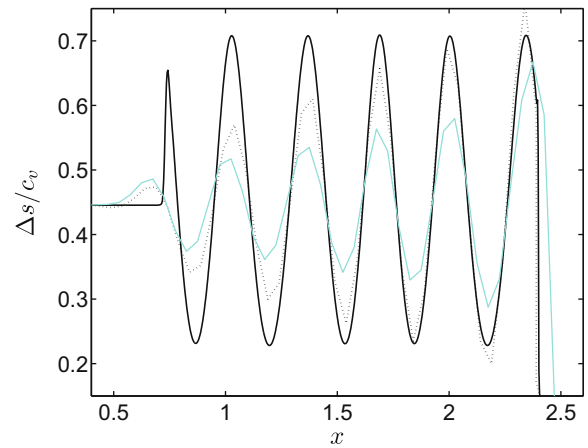


Fig. 3. Density profiles for the Shu–Osher problem with $\Delta x = 0.05$ at $t = 1.8$. The reference solution is the seventh-order accurate WENO solution with $\Delta x = 6.25 \times 10^{-3}$.



(a) *Hybrid, Stan, Stan-I, ADPDIS3D* and reference solutions.



(b) *Shock Fit, WENO* and reference solutions.

Fig. 4. Entropy profiles for the Shu–Osher problem with $\Delta x = 0.05$ at $t = 1.8$ (close-up of the solution just downstream of the shock). The reference solution is the seventh-order accurate WENO solution with $\Delta x = 6.25 \times 10^{-3}$.

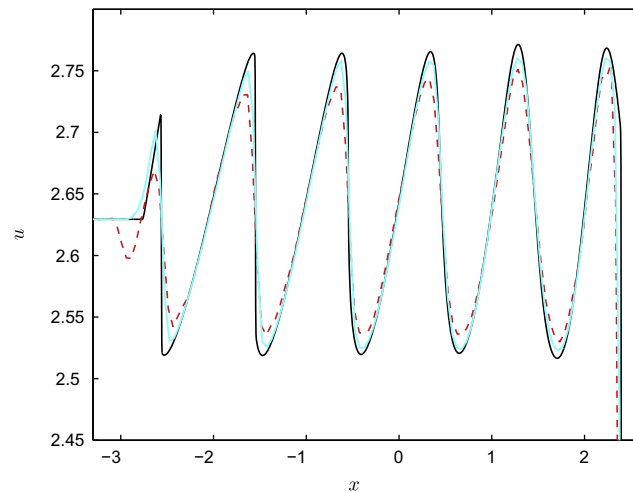


Fig. 5. Velocity profiles for the Shu–Osher problem using the *Stan* and *WENO* codes, with $\Delta x = 0.05$ at $t = 1.8$ (close-up of the solution just downstream of the shock). The reference solution is the seventh-order accurate WENO solution with $\Delta x = 6.25 \times 10^{-3}$.

schemes lies in the entropy waves; in order to visualize the important features of each method, the results are depicted in two different plots in Fig. 4. The different codes introduce various amounts of dissipation at the shock, so that the entropy wave just downstream of the shock has a different amplitude depending on the method. In fact, the *Shock Fit* code predicts the full entropy amplitude immediately behind the shock and even overshoots the reference solution, thus suggesting that the latter may not be completely converged at this particular location. Downstream of the shock, the entropy waves maintain their amplitudes for the non-dissipative methods (*Hybrid*, *ADPDIS3D*, *Stan-I* and *Stan*) but decrease as they propagate downstream for the dissipative methods (*WENO* and *Shock Fit*). This illustrates the fact that, while an accurate treatment of the shock is important, the properties of the numerics away from the shock also matter in order to achieve accurate results in the entire domain. There is little appreciable difference between the original and improved artificial diffusivity methods. This result confirms the underlying idea of Mani et al. [32] that a dilatation-based artificial bulk viscosity behaves similarly to the original one based on strain-rate magnitude at a shock wave. The methods relying on a bulk viscosity achieve higher amplitudes of the entropy waves than the other methods. This is an effect of the bulk viscosity only affecting the dilatational velocity field, whereas the upwinding-based methods add dissipation to all modes. The converse of this is seen in Fig. 5, which compares the acoustic waves for the most dissipative upwinding result (*WENO*) with the *Stan* code: for these waves, the *WENO* method is less dissipative.

3.3. Shock-vorticity/entropy wave interaction

A generalization of the Shu–Osher problem is the two-dimensional interaction of a vorticity/entropy wave with a normal shock [31]. The two-dimensional Euler equations are solved with $\gamma = 1.4$ on the domain $x_1 \in [0, 4\pi]$, $x_2 \in [-\pi, \pi]$, with $\Delta x_1 = \pi/50$ and $\Delta x_2 = \pi/16$. Periodic boundaries are used in the x_2 -direction; $x_1 = 0$ is a supersonic inflow and $x_1 = 4\pi$ is a subsonic outflow. Different techniques are employed to avoid acoustic reflections from the outflow, including an extension of the domain with a sponge region. First a one-dimensional base solution corresponding to a $M = 1.5$ shock is defined as

$$(\bar{\rho}, \bar{u}_1, \bar{p}) = \begin{cases} (\rho_L, u_L, p_L) = (1, 1.5, 0.714286), & x_1 < 3\pi/2, \\ (\rho_R, u_R, p_R) = (1.862069, 0.8055556, 1.755952), & x_1 \geq 3\pi/2. \end{cases} \quad (8)$$

A combined vorticity/entropy wave is superposed onto the base flow. The initial data then becomes

$$\rho = \bar{\rho} + \rho_L A_e \cos(k_1 x_1 + k_2 x_2), \quad (9a)$$

$$u_1 = \bar{u}_1 + u_L A_v \sin \psi \cos(k_1 x_1 + k_2 x_2), \quad (9b)$$

$$u_2 = -u_L A_v \cos \psi \cos(k_1 x_1 + k_2 x_2), \quad (9c)$$

$$p = \bar{p}, \quad (9d)$$

and the conditions at the inflow boundary $x_1 = 0$ are

$$\rho = \rho_L + \rho_L A_e \cos(k_2 x_2 - k_1 u_L t), \quad (10a)$$

$$u_1 = u_L + u_L A_v \sin \psi \cos(k_2 x_2 - k_1 u_L t), \quad (10b)$$

$$u_2 = -u_L A_v \cos \psi \cos(k_2 x_2 - k_1 u_L t), \quad (10c)$$

$$p = p_L. \quad (10d)$$

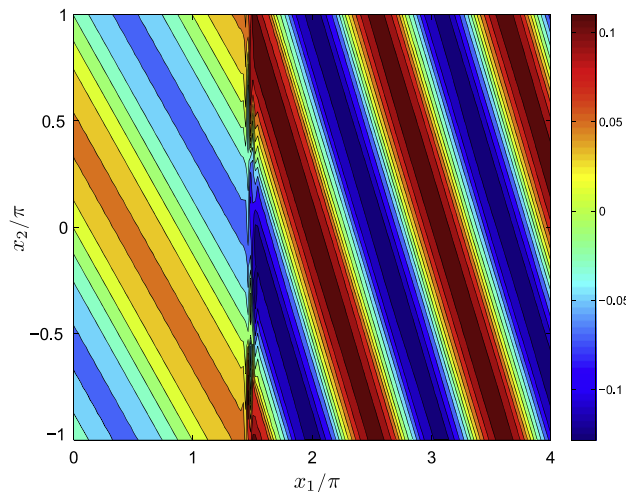
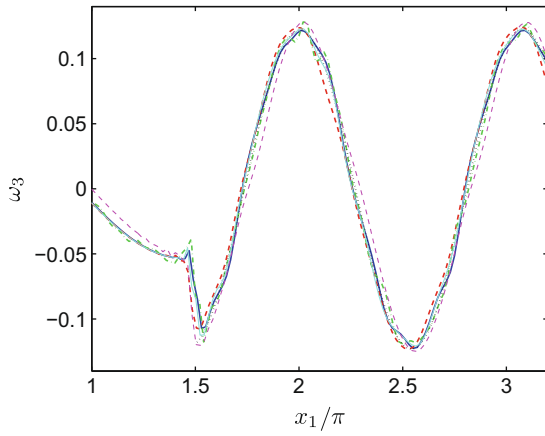
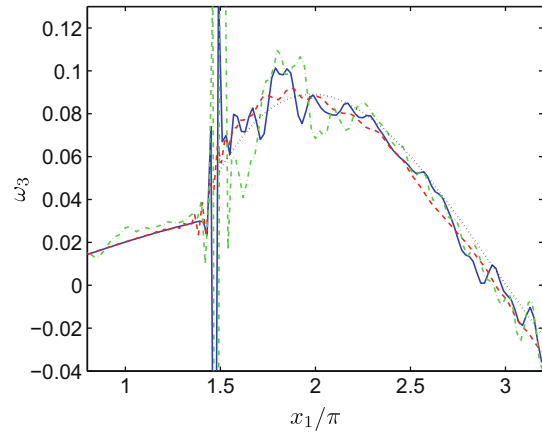
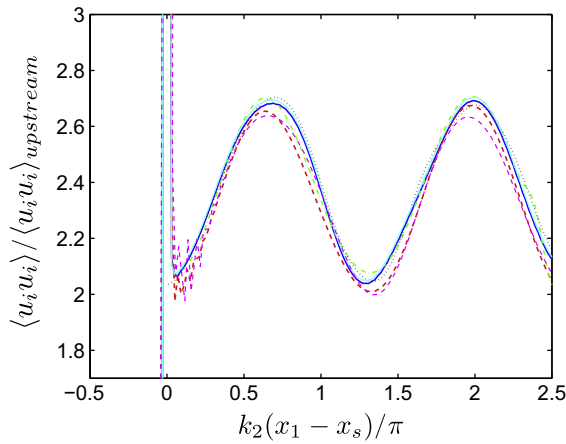
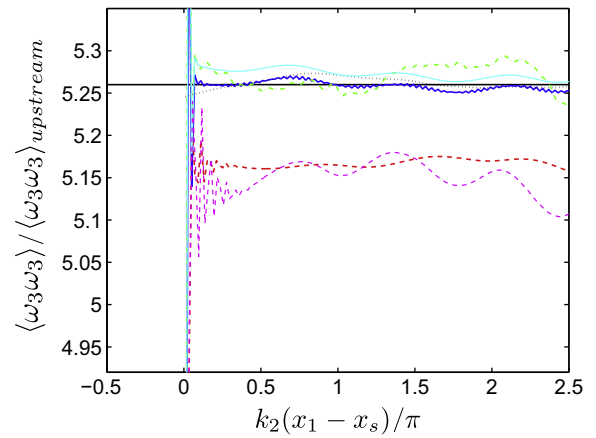
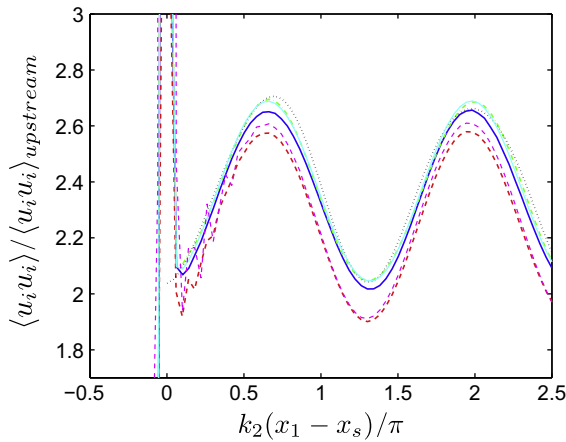
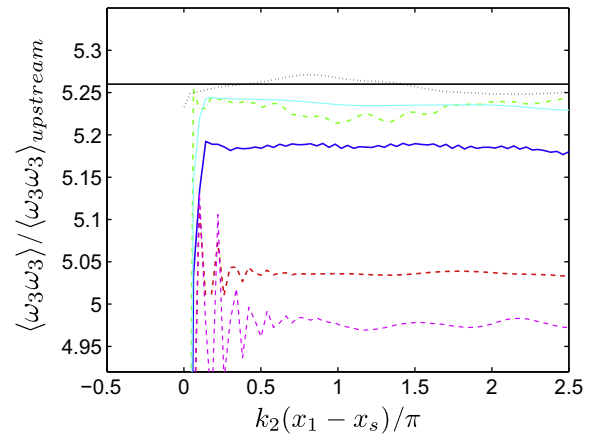


Fig. 6. Instantaneous vorticity contours for $\psi = 45^\circ$, $k_2 = 1$.

(a) $\psi = 45^\circ$ at $t = 25$.(b) $\psi = 75^\circ$ at $t = 32$. The results from the *WENO* and *Stan-I* codes are not shown, but are similar to those of the *Hybrid* and *Stan* codes, respectively.**Fig. 7.** Instantaneous vorticity profiles for the shock-vorticity/entropy wave interaction at $y = 0$ ($k_2 = 1$).(a) Kinetic energy ($k_2 = 1$).(b) Mean-square vorticity ($k_2 = 1$).(c) Kinetic energy ($k_2 = 2$).(d) Mean-square vorticity ($k_2 = 2$).**Fig. 8.** Mean quantities for the shock-vorticity/entropy wave interaction ($\psi = 45^\circ$). Shock location: $x_s = 3\pi/2$. The reference is the linear analysis solution of Mahesh [31].

For the present study,

$$k_1 = \frac{k_2}{\tan \psi}, \quad A_e = A_v = 0.025, \quad (11)$$

and $k_2 = 1, 2$. This inviscid problem has no length scale other than k_2 ; hence an increase of k_2 corresponds to an effectively coarser grid.

Fig. 6 shows instantaneous vorticity contours for $\psi = 45^\circ$ to provide a visual understanding of the problem. The vorticity waves coming from the left interact with the shock, become compressed and change their orientation. In order to compare the different codes, Fig. 7 shows instantaneous vorticity profiles through the domain for $k_2 = 1$ (the higher wavenumber plots look similar) for $\psi = 45^\circ$ and $\psi = 75^\circ$. All codes do well in the $\psi = 45^\circ$ case, but in the $\psi = 75^\circ$ case all codes except *Shock Fit* show evidence of post-shock oscillations. This behavior is discussed further in Section 4.2.1; here we simply note that the oscillations persist downstream for the codes without any linear dealiasing filters (*Hybrid* and *ADPDIS3D*), whereas the filter in the *Stan* codes removes these oscillations as they travel downstream.

Figs. 8 and 9 show the kinetic energy and mean-square vorticity downstream of the shock averaged in span and over one time period for $\psi = 45^\circ, 75^\circ$ and $k_2 = 1, 2$. The values are normalized with respect to the conditions upstream of the shock. There are slight differences in the mean shock position, implying a small phase difference downstream of the shock. In the $\psi = 45^\circ$ case, the vorticity seems to converge to the linearized solution for all codes as the grid is refined ($k_2 = 1$ is the effectively finer grid). The *Shock Fit* results are essentially identical between the two wavenumbers, which shows that the resolution of the post-shock region is sufficient (the shock-fitting method treats the shock analytically). The post-shock amplitudes of *WENO* and *ADPDIS3D* are similar, and slightly higher than that of the *Hybrid* code. The amplification occurs

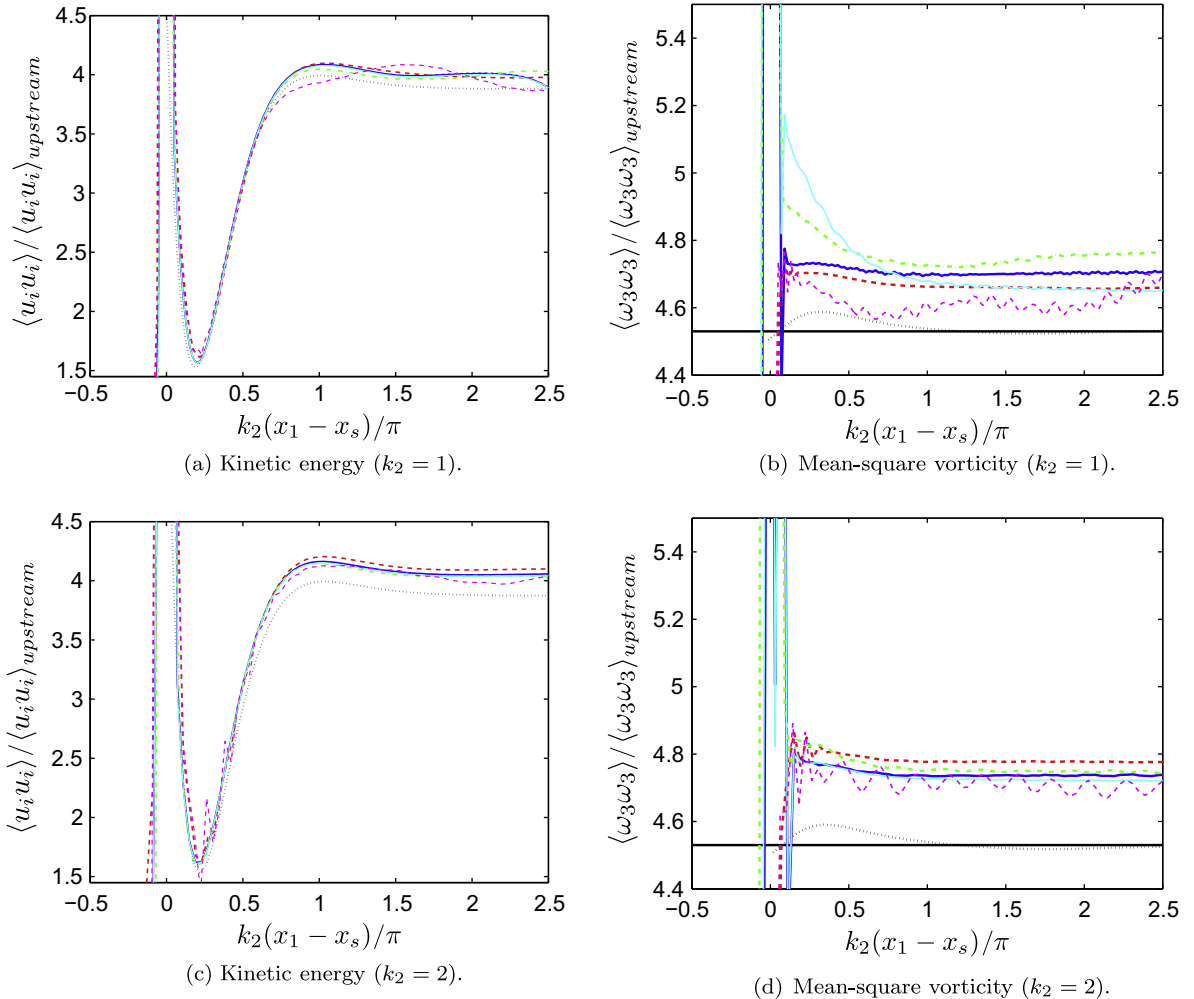


Fig. 9. Mean quantities for the shock-vorticity/entropy wave interaction ($\psi = 75^\circ$). Shock location: $x_s = 3\pi/2$. The reference is the linear analysis solution of Mahesh [31].

across the shock, which is effectively treated by seventh-order WENO in the former cases and by fifth-order WENO in the latter. Therefore, this difference illustrates that higher-order WENO schemes are better capable of capturing the interaction between a shock and a disturbance. In the $\psi = 75^\circ$ case, the codes all yield larger vorticity amplification than the linear analysis and seem to converge to a value different from the linearized solution; only the *Shock Fit* results agree well with the linear theory. Interestingly, all shock-capturing codes (i.e., except *Shock Fit*) yield higher amplifications on the effectively coarser grid; this behavior is most likely related to the post-shock oscillations. These issues are discussed further in Section 4.2.1.

3.4. Noh problem

The Noh problem [34] consists of an infinite Mach number implosion and is relevant to inertial confinement fusion, in which strong shock waves interact with interfaces separating different fluids and with the resulting turbulence. The goal of this problem is to test the capability to handle a strong spherical shock. In particular, this problem provides an assessment of the capability to predict the post-shock density (i.e., the compression by the strong shock wave), the correct shock speed, and the spherical shape on a Cartesian grid (i.e., whether grid-imprinting errors are generated).

The three-dimensional Euler equations with $\gamma = 5/3$ are solved on the domain $x_i \in [0, 0.256]$ with $\Delta x_i = 0.002$ and symmetry conditions imposed along $x_i = 0$. The remaining boundaries are supersonic inflows where the velocity and pressure from the initial conditions are imposed, and the time-dependent density is set from the analytical solution. The initial conditions correspond to a spherically imploding flow with uniform density and pressure:

$$\rho = 1, \quad (12a)$$

$$u_i = -x_i/r, \quad (12b)$$

$$p = \epsilon, \quad (12c)$$

where $r = \sqrt{x_i x_i}$. The pressure is nominally zero and leads to an infinite Mach number for the imploding flow. To prevent complex eigenvalues (which would make the problem ill-posed), a lower bound on the pressure is imposed as $p_{\min} = \epsilon = 10^{-6}$.

In response to the initial imploding flow, a strong spherical shock wave traveling outward at constant speed develops. The analytical solution for the density in three dimensions is [34]

$$\rho = \begin{cases} 64, & r < t/3, \\ (1 + t/r)^2, & r \geq t/3. \end{cases} \quad (13)$$

Shown in Fig. 10 are profiles of the density along and diagonal to the grid. The *Hybrid* results are the closest to the analytical solution, with small errors in both the shock location and the spherical shape. The *Stan* and *Stan-I* codes yield larger errors in shock position and post-shock density, and larger grid imprinting errors near the origin. The original form of the bulk viscosity (*Stan*) gives a somewhat smaller error in shock position compared to the “improved” version (*Stan-I*). We note that the results from the artificial diffusivity methods for this problem in Ref. [8] are significantly better than the *Stan* results

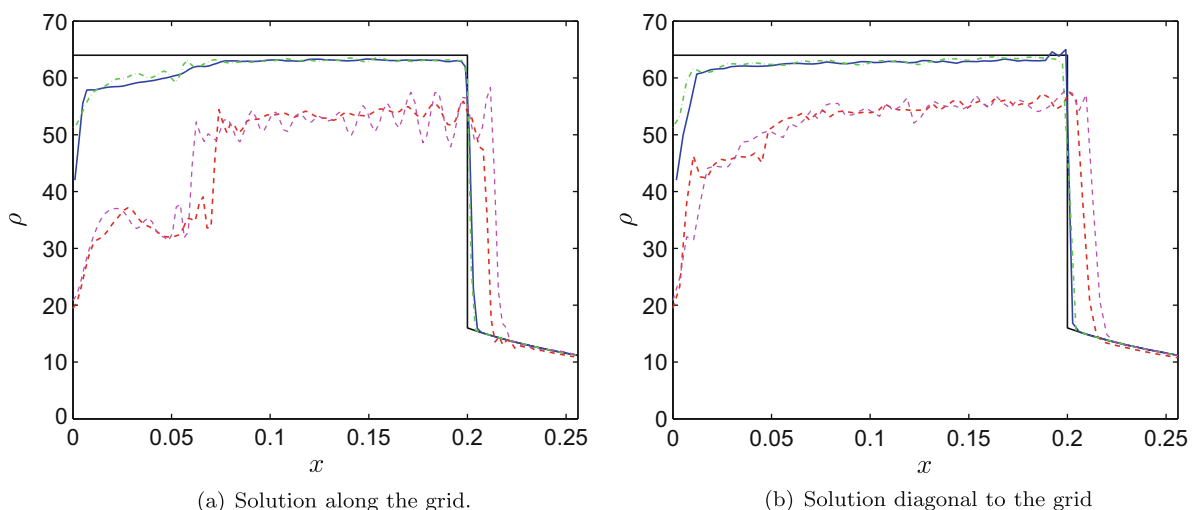


Fig. 10. Profiles at $t = 0.6$ for the Noh problem. The *WENO* method is not shown for clarity, but is slightly better than the *Hybrid* method; the results from the *ADPDIS3D* code are based on the divergence form of the convective terms with the addition of a 10th-order accurate linear dissipation. The reference is the analytical solution of Noh [34].

Table 4

Accuracy metrics for the Noh problem.

	<i>Hybrid</i>	<i>ADPDIS3D</i>	<i>Stan</i>	<i>Stan-I</i>	<i>WENO</i>	Exact
Noh mean density	63.2	63.3	55.1	54.9	63.3	64.0
Noh rms density	0.374	0.238	0.630	0.814	0.346	0.000

(roughly halfway between the *Stan* and *Hybrid* results on equivalent grids). The main difference between *Stan* results and those of Cook and Cabot [8] is that the former treats the convective terms on a split form; this difference is most likely to blame for the worse results by the *Stan* code. As described in Section 2.2.4 on the *ADPDIS3D* code, when the un-split form of the convective terms and a 10th-order linear dissipation are used for the base scheme step, a stable solution could be obtained.

In order to provide a quantitative comparison of the codes, the mean density in the spherical shell $r \in [0.15, 0.17]$ at $t = 0.6$ is listed in Table 4; this quantity provides a measure of the compression achieved downstream of the shock. The RMS of the density fluctuations in the same spherical shell is also listed in the table; this quantity provides a measure of the grid-imprinting errors. The spherical shell is chosen such that errors near the center and near the shock do not affect this value. The purpose of listing these metrics is to provide quantitative means for other researchers to evaluate their codes against the present algorithms.

One should note that the errors in shock position and post-shock density are related to each other through mass conservation since all the methods are discretely conservative. Assume a correct shock location at some time t ; then the pre-shock density is determined by the smooth analytical solution, as is the radial mass flux. If the compression by the shock is underpredicted, then the post-shock density is by definition also underpredicted. To conserve mass, this implies that the shock speed must be overpredicted, thereby leading to the shock location being overpredicted for all subsequent times.

Finally, the *WENO* results are not shown here since they are very similar to the *Hybrid* results (though there are slight differences in the metrics in Table 4). For this problem the shock sensor in *Hybrid* is activated almost everywhere for the entire calculation. This effect illustrates that there is no universal shock sensor; a different sensor design may be able to confine the *WENO* procedure to the shock region only e.g., the sensor by Hill and Pullin [18] works well for this problem. Results from the *Shock Fit* code are not included because there is initially no well-defined shock.

3.5. Compressible isotropic turbulence

The final test case is that of decaying compressible isotropic turbulence with eddy shocklets [27]. Given a sufficiently high turbulent Mach number M_t , weak shock waves (eddy shocklets) develop spontaneously from the turbulent motions. The goal of this problem is to test the ability of the methods to handle ‘randomly’ distributed shocklets (in the sense of the shock locations not being known a priori), as well as the accuracy for broadband motions in the presence of shocks.

The three-dimensional Navier–Stokes equations with $\gamma = 1.4$ are solved on the domain $\mathbf{x}_i \in [0, 2\pi]^3$ with grid spacing $\Delta x_i = 2\pi/64$ and periodic boundary conditions in all directions. The (physical) viscosity is assumed to follow a power-law of the type

$$\frac{\mu}{\mu_{\text{ref}}} = \left(\frac{T}{T_{\text{ref}}} \right)^{3/4}. \quad (14)$$

The important parameters are the turbulent Mach number and Taylor-scale Reynolds number defined as

$$M_t \equiv \frac{\sqrt{\langle u_i u_i \rangle}}{\langle c \rangle}, \quad Re_\lambda \equiv \frac{\langle \rho \rangle u_{\text{rms}} \lambda}{\langle \mu \rangle}, \quad (15)$$

where

$$u_{\text{rms}} \equiv \sqrt{\frac{\langle u_i u_i \rangle}{3}}, \quad \lambda^2 \equiv \frac{\langle u_i^2 \rangle}{\langle (\partial_1 u_1)^2 \rangle}. \quad (16)$$

The initial condition consists of a random solenoidal velocity field $u_{i,0}$ that satisfies

$$E(k) \sim k^4 \exp(-2(k/k_0)^2), \quad \frac{3u_{\text{rms},0}^2}{2} = \frac{\langle u_{i,0} u_{i,0} \rangle}{2} = \int_0^\infty E(k) dk. \quad (17)$$

The chosen energy spectrum yields $\lambda_0 = 2/k_0$, where k_0 is the most energetic wavenumber, taken as $k_0 = 4$ here. Full details required to generate the initial conditions are included in Appendix A. The density and pressure fields are initially constant, with the initial parameters, $M_{t,0} = 0.6$ and $Re_{\lambda,0} = 100$. Since the initial conditions are not in acoustic equilibrium, a field of background acoustic waves develops and persists throughout the simulation. Similarly, there are initial entropy modes. We note that this particular initial condition is chosen since, for the present comparison, a problem with large acoustic and entropy modes is desirable to highlight the performance of the methods. In order to generate the reference solution,

the *Hybrid*, *ADPDIS3D* and *Stan* codes were run on a sequence of grids up to 256^3 . All the present methods converge on the finest grid, and agreed with each other even on a point-wise basis at the final time $t/\tau = 4$, where $\tau = \lambda_0/u_{\text{rms},0}$ is the eddy turn-over time. We note as an aside that this point-wise agreement after four turn-over times implies that the divergence of different trajectories in this chaotic dynamical system is significantly slower than the characteristic turbulence time scale.

The temporal evolution of the mean-square velocity and vorticity, and the variance of the temperature and dilatation are plotted in Fig. 11. The RMS of pressure and density exhibit a behavior similar to that of temperature and are therefore not shown. The minimally dissipative *Hybrid* code agrees well with the reference solution for all quantities. The *WENO* code underpredicts all quantities, thereby showing how dissipative it is for broadband motions. It particularly underpredicts the vorticity and dilatation, which is consistent with the fact that the *WENO* procedure damps the small-scale motions. The *ADPDIS3D* code agrees with the reference almost as well as the *Hybrid* code except that it is more dissipative. The original and improved artificial diffusivity methods behave similarly for the kinetic energy and the enstrophy, but the original method (*Stan*) is highly dissipative for both dilatational and temperature fluctuations; in fact, it annihilates the dilatational motions very quickly. It was this finding that spurred Mani et al. [32] and subsequent researchers to improve the method by making the artificial bulk viscosity sensitive to dilatational motions; the improvement in the dilatation fields of the *Stan-I* code over those of the *Stan* code is solely due to this implementation of the artificial bulk viscosity. Similarly, the predicted temperature fluctuations are significantly improved. Additional information on the artificial diffusivity methods are provided in Appendix C.

Instantaneous profiles of dilatation, density, temperature and vorticity through an eddy shocklet are shown in Fig. 12. The shocklet is located at $x_1 \approx 2.8$, i.e., at the point of large negative dilatation. The *Hybrid*, *ADPDIS3D* and *Stan-I* codes exhibit a

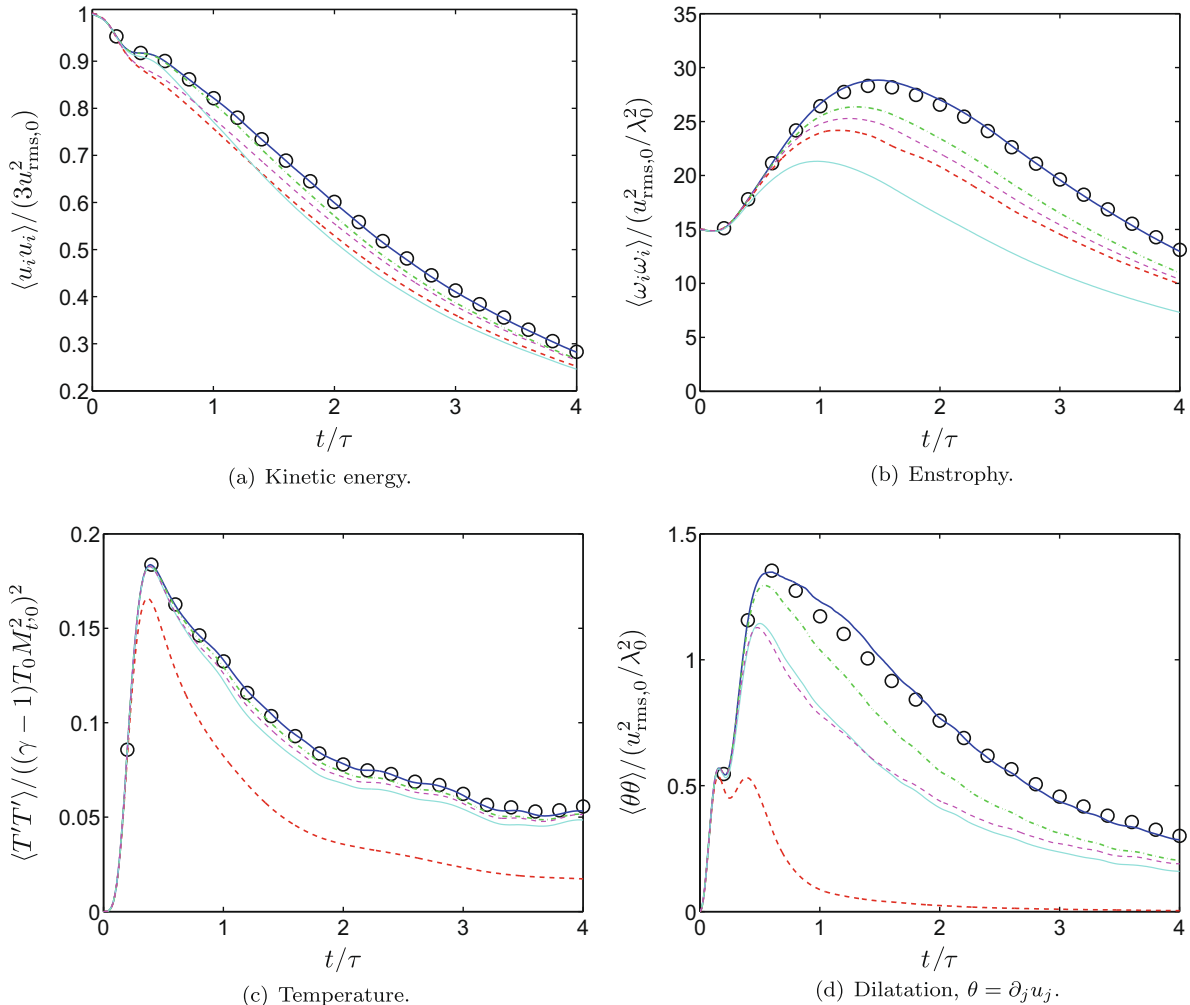


Fig. 11. Temporal evolution of the variance of different quantities for the isotropic turbulence problem on 64^3 grid. The reference is the solution on a 256^3 grid spectrally filtered to a 64^3 grid (circles).

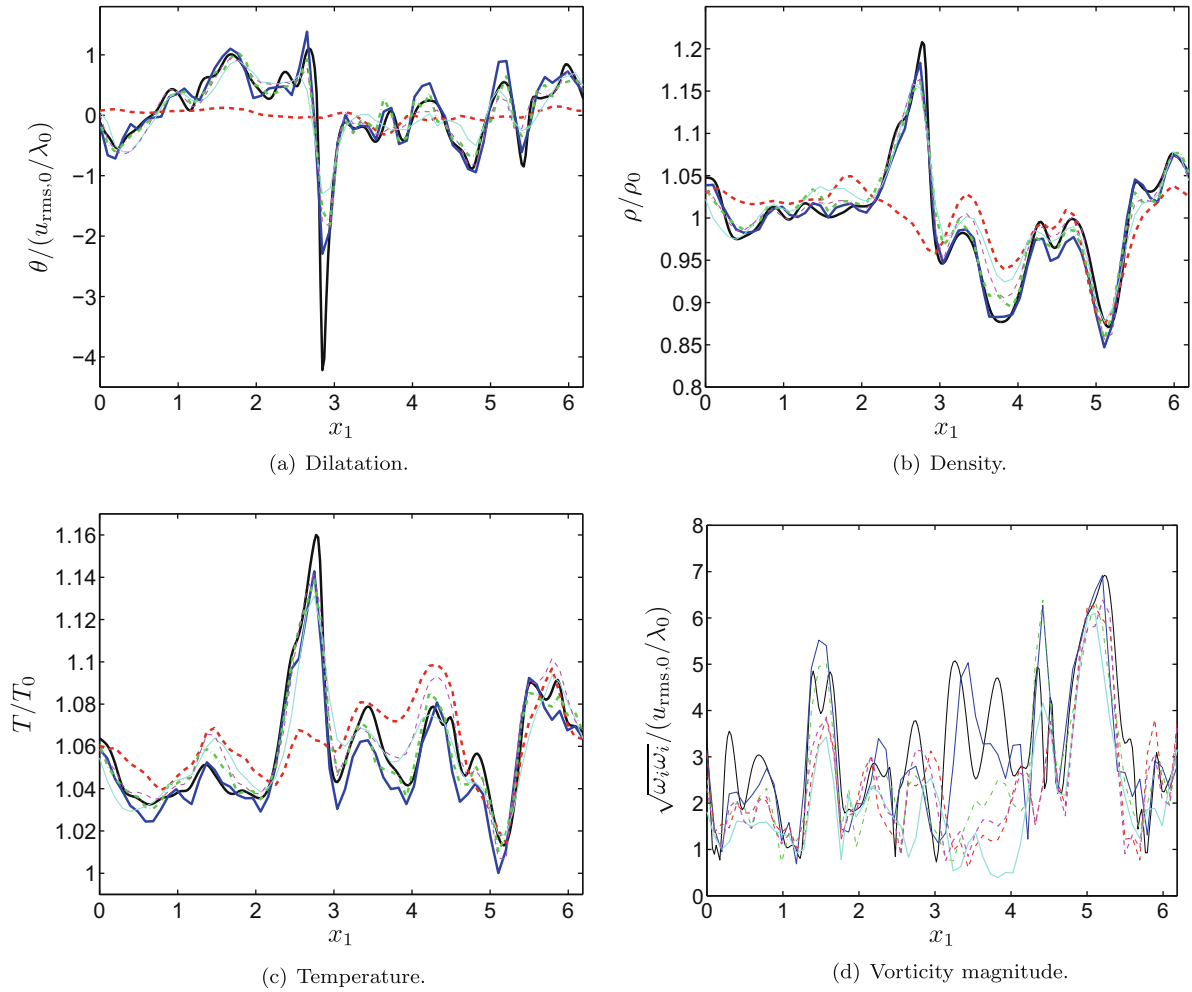


Fig. 12. Instantaneous profiles through a shocklet (at $x_s \approx 2.8$) for the isotropic turbulence problem on 64^3 grid at $t/\tau = 4$. The reference is the unfiltered solution on a 256^3 grid.

reasonable behavior compared to the converged solution, as does the WENO method despite its larger numerical dissipation. The annihilation of dilatational motions by the original formulation of the artificial bulk viscosity is clear: not only is the eddy shocklet wiped out, but so are the background acoustic waves. Nevertheless, the method *does* preserve the peaks in the vorticity profile, which shows that the original artificial diffusivity method is capable of handling vortical motions; this is consistent with the reasonable results obtained for the Taylor–Green problem.

Finally, the velocity, vorticity, dilatation and density spectra are plotted in Fig. 13. The results for the velocity and vorticity spectra agree well with the previous findings for the Taylor–Green problem. The dilatation and density spectra agree qualitatively with each other and illustrate how the artificial bulk viscosity affects more than just the dilatational motions. The improvement from *Stan* to *Stan-I* is substantial. The *Stan* code not only damps small-scale fluctuations, but ominously even damps the very largest scales in the domain. The reason for this behavior can be traced to the (lack of) localization of the bulk viscosity to regions containing shocks. In theory, the method should introduce artificial bulk viscosity only near shocks; this is the case for “pure” shock problems like the Shu–Osher, shock-vorticity, and Noh problems in this study. In the isotropic turbulence problem, however, the strain-rate-based artificial bulk viscosity is large everywhere in the domain. This is illustrated in Fig. 14, which plots the normalized artificial bulk viscosity through the eddy shocklet considered in Fig. 12 for two different grid resolutions for both the *Stan* and *Stan-I* codes. The amount of artificial bulk viscosity is equally large everywhere in the domain, and the shocklet is clearly not detected. The latter is consistent with the much faster than linear decrease of the bulk viscosity under grid refinement. In contrast, the improved *Stan-I* method yields a much lower artificial bulk viscosity throughout the domain, and the shocklet is clearly detected. Under grid refinement, the improved method yields a rapid decrease away from the shocklet and a much slower decrease at the shocklet – this is how the algorithm is intended to behave.

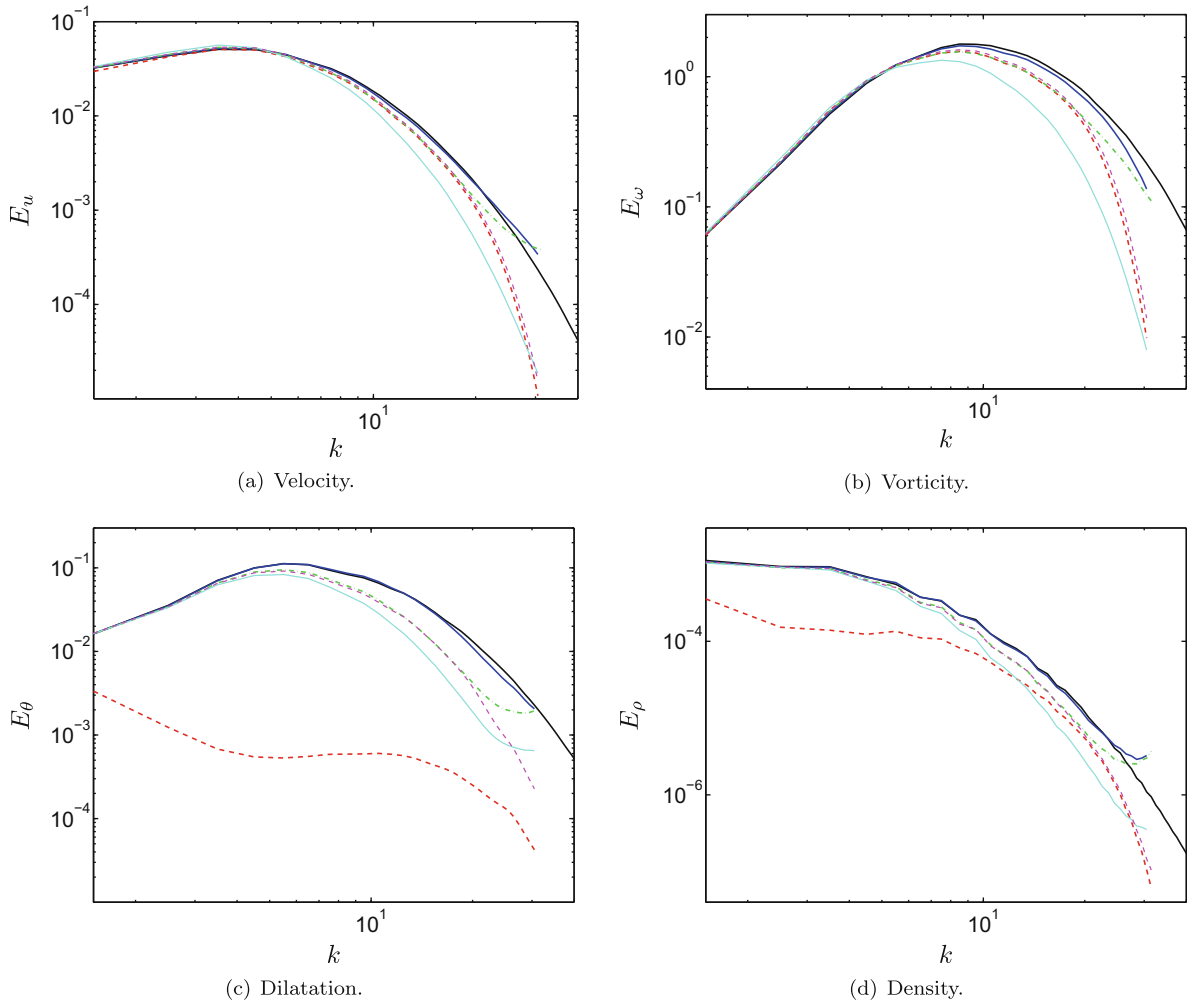


Fig. 13. Spectra at $t/\tau = 4$ for the isotropic turbulence problem on a 64^3 grid. The reference is the solution on a 256^3 grid.

4. Discussion

4.1. Effective bandwidth

One measure of efficiency of the methods under consideration is the range of wavenumbers that are resolved accurately. Simply put, for a higher maximum accurately resolved wavenumber, a coarser grid could be used to achieve a given overall accuracy. To quantify the effective bandwidth of the schemes we consider the following compensated spectrum

$$\tilde{E}(k) = \frac{E(k)}{E_{\text{conv}}(k)}, \quad (18)$$

where $E(k)$ is the spectral density at wavenumber k on a given grid, and $E_{\text{conv}}(k)$ is the converged spectrum. This quantity is shown in Fig. 15 for the Taylor–Green vortex and isotropic turbulence on 64^3 grids. The bandwidth is quantified by the wavenumber k_c where the deviation from the reference is 25%. Though this limit is arbitrary, it is chosen so that it is larger than the 10% maximum deviation between the dissipative and non-dissipative reference spectra from the different methods. It should be noted that the Taylor–Green vortex is inviscid so that any dissipation is numerical, while viscosity is present in the isotropic turbulence problem, thereby providing physical dissipation that affects the spectra.

For each method, the behavior of the compensated spectrum is similar for the two problems. For the *WENO* method, a bandwidth of $k_c \approx 0.25 k_{\text{max}}$ is achieved in both problems. The *Hybrid* method yields a pile-up at the highest wavenumbers in both cases, with $k_c \approx 0.6 k_{\text{max}}$ and $k_c \approx 0.8 k_{\text{max}}$ for the two problems, respectively. The *ADPDIS3D* code is similar. The very high value of $k_c \approx 0.8 k_{\text{max}}$ for the *Hybrid* and *ADPDIS3D* codes on the isotropic turbulence problem should be interpreted as being the result of a balance between viscous dissipation and aliasing error pile-up; hence $k_c \approx 0.6 k_{\text{max}}$ from the

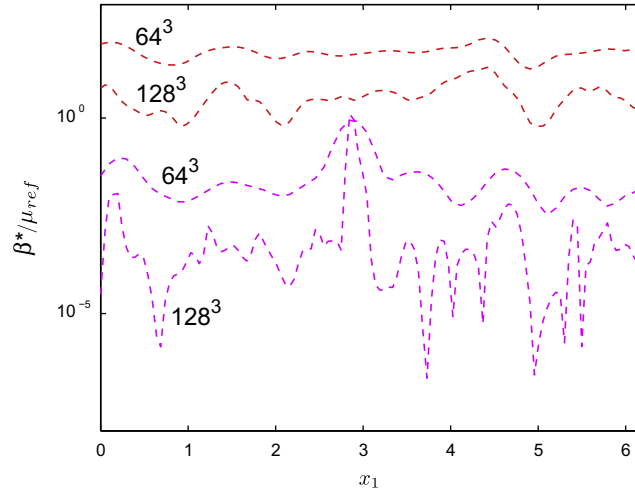


Fig. 14. Instantaneous bulk viscosity profile through a shocklet (at $x_s \approx 2.8$) for the isotropic turbulence problem on 64^3 and 128^3 grids at $t/\tau = 4$, using the *Stan* and *Stan-I* codes.

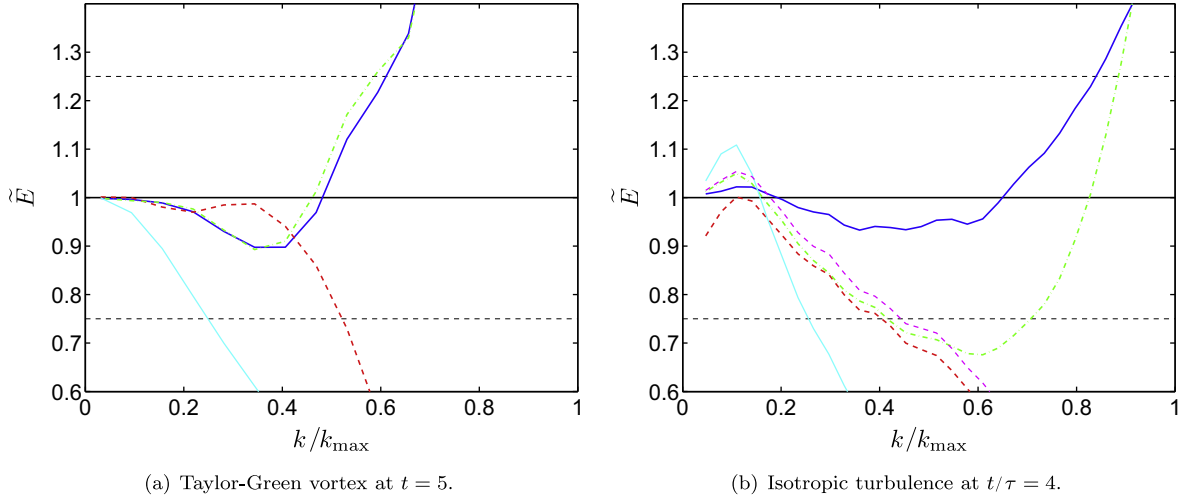


Fig. 15. Compensated spectra on a 64^3 grid. As a reminder, *Stan* is dashed red, *Stan-I* is dashed magenta (thin), *Hybrid* is solid blue, *WENO* is solid cyan (thin), and *ADPDIS3D* is dash-dotted green. (For interpretation of the references to colour in this figure legend, the reader is referred to the web version of this article.)

Taylor–Green vortex is a more fair result for these codes. Both the original *Stan* and improved *Stan-I* methods yield $k_c \approx 0.5 k_{max}$ on both problems (recall that they are identical for the Taylor–Green vortex). The similarity between these methods for the isotropic turbulence problem is simply an effect of the velocity fluctuations being dominated by solenoidal and vortical motions, which are not affected directly by the artificial bulk viscosity. The fact that the effective bandwidth is $0.5 k_{max}$ is at first surprising, since both the dealiasing filter and the artificial shear viscosity (which acts on vortical motions) are designed to affect only the highest wavenumbers. The reason is either that the cumulative effect over many time steps of these dissipation operators is significantly larger than the single-pass effect, or that nonlinear interactions redistribute the damping to lower wavenumbers. Most likely, both effects are important.

These numbers have important implications on the computational cost: if one wants to resolve a given wavenumber range with *WENO*, more than twice as many grid points are required in every direction. With explicit time stepping, this implies more than a factor of 16 higher computational cost. This is a significant drawback.

4.2. Shock sensor

The *Hybrid* method relies on a flow sensor to identify any shocks. The comprehensive set of test cases in the present study has illuminated how difficult it is to design a “universal” shock sensor, i.e., one that works well for general problems. When

turbulence is present, the dilatation/vorticity sensor inspired by Ducros et al. [11] was found to work well. The sensor loses its meaning whenever vorticity is not present, and reverts to identifying every region of flow compression. Hence, the sensor marks the whole pre-shock domain in the Noh problem, for example; while this behavior does not affect the results for this particular problem, the sensor is clearly not suited to it. In addition, the sensor was found to behave erratically on very coarse grids, where the vorticity is poorly captured (data not shown). Lastly, we found that the sensor operates better when the vorticity in the denominator is averaged in some sense (locally, or in homogeneous directions), since this prevents marking random regions of small vorticity as “shocks”.

The flow sensor by multiresolution wavelet analysis of the computed flow data in the *ADPDIS3D* code is more flexible. By computing wavelet coefficients of a given grid function (with a suitable set of wavelet basis functions), we obtain very precise information about the regularity of the grid function (computed flow data) in question. This information is obtained by simply analyzing a given grid function. No information about the specific problem being solved is required. Thus, wavelet detectors are general, problem-independent and rest on a solid mathematical foundation. One of the challenges for the adaptive filter method is a universal multiresolution wavelet that works well for shocks, spurious oscillations and turbulent fluctuations.

Finally, the sensor of Hill and Pullin [18] that is based on the WENO smoothness indicators of the density field was tested in this study, and was found to yield stable solutions on all problems at the price of prematurely activated dissipation (data not shown). One advantage of this sensor (compared to the Ducros-sensor) is that it is also capable of finding both contact and material discontinuities.

4.2.1. Post-shock oscillations in the shock-vorticity/entropy wave interaction

In the shock-vorticity/entropy wave interaction, significant post-shock oscillations are observed downstream of the shock for the case $\psi = 75^\circ$. These errors are similar to the so-called *slow-shock* or *post-shock* oscillations found to occur primarily when a shock is moving slowly relative to the grid [2]. That these errors are post-shock oscillations was inferred in several ways. First, they do not disappear under grid or time step refinement, and their amplitude decreases when the order of accuracy of the methods is decreased (e.g., changing from seventh to fifth-order accurate WENO). Second, the oscillations disappear if the reference frame is changed such that the shock is moving through the domain more rapidly. Finally, the lack of post-shock oscillations in the *Shock Fit* results, where the shock is treated analytically, implies that the capturing of the shock is to blame.

Though post-shock oscillations were first reported in a two-dimensional problem [47], most of the subsequent analysis has been done in one-dimensional settings. In these one-dimensional studies, it is argued that the post-shock oscillations are strongly tied to the shock velocity relative to the grid, and that significant post-shock oscillations occur if the shock speed is much smaller than the maximum wavespeed in the domain, i.e., if it takes several time steps for the shock to cross a single grid cell [28]. In the present study, the shocks traverse each grid point in approximately 16 time steps in both the $\psi = 45^\circ$ and $\psi = 75^\circ$ cases. However, only the latter show signs of post-shock oscillations. This suggests that the shock speed is not the only criterion in the generation of post-shock oscillations, but that there may be multi-dimensional effects as well. From a physical point of view, the difference between the two cases is that the smaller angle leads to a propagating acoustic field behind the shock, whereas the larger angle has an evanescent pressure field; it is possible that this difference in physics plays a role in determining whether post-shock oscillations are generated, though further study is clearly necessary.

We also note that Mahesh [31] argued that the difference between his results and the linear analysis (at $\psi = 75^\circ$) was that the linear theory is not valid for that angle due to transonic effects. However, the present *Shock Fit* results agree perfectly with linear theory; hence the discrepancy in [31] was most likely due to post-shock oscillations, as illustrated in the present results, in which the mean-square vorticity calculated from the simulations overpredicts the linear theory.

4.3. Shock fitting

The Shu–Osher problem and the shock-vorticity/entropy wave interaction are ideal for shock fitting because of the well-defined shocks that maintain their topology throughout the simulation. In these problems, results from the shock fitting scheme have been found to be accurate and free of spurious oscillations for problems involving shocks and disturbances. There are obvious advantages to using a shock-fitting method for strong well-defined shocks in a simple geometry where the flow behind the shock is smooth. However, for more realistic problems in which no well-defined shocks are present initially or in which multi-dimensional shock interactions occur, the application of the present shock fitting approach is more challenging. In addition, the Shu–Osher results clearly show that the numerics away from the shock matter as well. Therefore, the shock fitting code should be combined with a minimally dissipative method that is capable of capturing shocks, allowing for strong well-defined shocks to be handled analytically while weaker, more random shocks could be captured. Work done on the aforementioned idea will be reported on a forthcoming paper.

5. Conclusions

The objective of the present work is to evaluate the performance of several numerical methods on problems in which shock waves and turbulence are present and interact dynamically. Several different numerical methods (WENO, hybrid

WENO/central difference, artificial diffusivity, adaptive characteristic-based filter and shock fitting) for compressible turbulence are assessed on under-resolved grids. A wide range of discriminatory problems is considered, including purely broadband (Taylor–Green vortex), shock-dominated (Shu–Osher problem, shock-vorticity/entropy wave interaction, Noh problem), and a combination of the two (compressible isotropic turbulence). Even though qualitatively different behavior is observed in some cases, all the schemes perform well for most of the test problems. The following observations are made:

- The WENO method provides sharp shock capturing, but overwhelms the physical dissipation and underpredicts approximately the upper 3/4 of the resolvable wavenumbers for broadband problems.
- The artificial diffusivity method of Cook [6] performs well on the problems with either shocks or broadband motions, but vastly underpredicts the dilatational velocity and thermodynamic (density, pressure, temperature) fluctuations when shocks and turbulence are interspersed; in fact, even WENO yields better results for the dilatation and thermodynamic fluctuations. The reason for this behavior is that the artificial bulk viscosity is based on the strain-rate magnitude, such that its value is both large and rapidly varying in turbulent regions. Hence, this formulation leads to a large bulk viscosity, which in turn annihilates dilatational motions. This behavior is improved by re-defining the artificial bulk viscosity to be a function of the dilatation.
- The Noh problem illustrates how the use of a split ('skew-symmetric') scheme negatively affects the capturing of a strong shock: it decreases the shock compression in the artificial diffusivity method. The hybrid WENO/central difference method avoids this issue by switching to a conservative formulation in the WENO region.
- Severe post-shock oscillations are found in the two-dimensional shock-vorticity/entropy wave interaction. While this issue has primarily been studied in a one-dimensional context to date, the results indicate that there are multi-dimensional effects as well. All shock-capturing methods tested here generate post-shock oscillations, although methods with dealiasing filters reduce their magnitude downstream of the shock. Interestingly, the present results suggest that the poor agreement between linear analysis and computations for the larger angle in [31] was due to post-shock oscillations, not invalidity of the linear analysis.
- The shock fitting approach avoids post-shock oscillations and yields superior results immediately downstream of the shock. The results also show that shock fitting must be coupled with minimally dissipative numerics, as illustrated by the significant dissipation away from the shock in the Shu–Osher problem.
- The comprehensive nature of the test problems in this study proved to be a challenge in terms of defining a shock sensor in the hybrid WENO/central difference method. The dilatation/vorticity sensor works adequately for these problems, although it does so in an unintended way for the turbulence-free problems.
- The compressible isotropic turbulence problem with eddy shocklets proved to be a challenging problem because weak shocks are interspersed with turbulence and all compressible modes (vortical, entropic, acoustic) are present.

Based on these observations, we can make the following recommendations:

- WENO and the original artificial diffusivity method of Cook [6] in their standard forms are not suitable for high-fidelity computations of compressible turbulence. If used, they must be accompanied with convincing grid refinement studies clearly showing sufficient grid resolution. While this statement is true for every method, it is particularly true for highly dissipative methods. Simply showing that spectra are decaying at the highest wavenumbers is not sufficient, since this is a built-in feature of dissipative methods.
- The modified artificial diffusivity methods that use dilatation rather than strain-rate magnitude to activate the artificial bulk viscosity are substantial improvements over the original method of Cook [6], and make the method suitable for compressible turbulence calculations.
- The benefits of minimizing numerical dissipation (e.g., by restricting the regions in which it is applied) are clear. The main challenge for the hybrid central/WENO method lies in the shock sensor.
- The main advantage of shock fitting (over shock-capturing) is that it avoids post-shock oscillations. The main challenge is that it is difficult to apply to shocks with complex and/or changing topology.

Acknowledgments

The authors wish to thank Dr. A. Cook for his help in defining the test problems and for discussions of the results, and Dr. S. Kawai and Dr. A. Mani for insightful conversations on artificial diffusivity methods. This work was supported by DOE-Sci-DAC (Grant DE-FC02-06-ER25787).

Appendix A. Initial conditions for the compressible isotropic turbulence problem

The procedure to generate the random initial solenoidal velocity field for the isotropic turbulence problem is described in this section. In the present comparative study, the initial density and pressure fields are taken to be constant, although a

more physically realistic initial condition can be obtained by combining the random velocity field described here with the method by Ristorcelli and Blaisdell [36] to find the pressure, density and dilatational velocity fields.

The initial velocity field is given in terms of its Fourier coefficients as

$$\hat{\mathbf{u}}(k_1, k_2, k_3) = \left(\frac{k_2}{k_{12}} a + \frac{k_1}{k_{12}} \frac{k_3}{k} b, \frac{k_2}{k_{12}} \frac{k_3}{k} b - \frac{k_1}{k_{12}} a, -\frac{k_{12}}{k} b \right), \quad (19)$$

where k_i are the wavenumbers, $k = \sqrt{k_i k_i}$ is the wavenumber magnitude, and $k_{12} = \sqrt{k_1^2 + k_2^2}$. This is valid for all wavenumbers other than $(0, 0, 0)$ provided one defines that $k_1/k_{12} = 0$ and $k_2/k_{12} = 1$ for $k_{12} = 0$. The quantities a and b are

$$a = \sqrt{\frac{2E(k)}{4\pi k^2}} e^{i\varphi_1} \cos \varphi_3, \quad b = \sqrt{\frac{2E(k)}{4\pi k^2}} e^{i\varphi_2} \sin \varphi_3, \quad (20)$$

where φ_1 , φ_2 , and φ_3 are random numbers uniformly distributed on $[0, 2\pi)$ that are re-sampled for each wavenumber triplet. The energy spectrum function is

$$E(k) = u_{\text{rms}}^2 16 \sqrt{\frac{2}{\pi}} \frac{k^4}{k_0^5} \exp(-2k^2/k_0^2), \quad (21)$$

where k_0 is the most energetic wavenumber. The energy spectrum function integrates to

$$\frac{3u_{\text{rms}}^2}{2} = \int_0^\infty E(k) dk. \quad (22)$$

Note also that the initial Taylor length scale is $\lambda_0 = 2/k_0$.

Appendix B. Numerical methods

This section further provides descriptions of the different methods. The reader is referred to the original references for additional details. Without loss of generality, we consider the one-dimensional form of Eq. (1):

$$\frac{dq}{dt}\bigg|_i = -\frac{\partial f}{\partial x}\bigg|_i, \quad (23)$$

where q is the vector of conserved variables and f is the flux. Boldface is not used for simplicity, but is implied.

In all problems, all methods satisfy the CFL condition for the given discretizations. Time-marching errors are not expected to play a role in the present study; we did not seek to optimize the time stepping.

B.1. The Stan code

In the *Stan* code, a sixth-order accurate compact finite difference scheme optimized for high-wavenumber resolution [30] is used to compute first derivatives,

$$\beta_1 f'_{i-2} + \alpha_1 f'_{i-1} + f'_i + \alpha_1 f'_{i+1} + \beta_1 f'_{i+2} = c_1 \frac{f_{i+3} - f_{i-3}}{6\Delta x} + b_1 \frac{f_{i+2} - f_{i-2}}{4\Delta x} + a_1 \frac{f_{i+1} - f_{i-1}}{2\Delta x}, \quad (24)$$

where $\alpha_1 = 0.5381301$, $\beta_1 = 0.0666332$, $a_1 = 1.3675777$, $b_1 = 0.8234282$, and $c_1 = 0.0185208$, and second derivatives,

$$\beta_2 f''_{i-2} + \alpha_2 f''_{i-1} + f''_i + \alpha_2 f''_{i+1} + \beta_2 f''_{i+2} = c_2 \frac{f_{i+3} - 2f_i + f_{i-3}}{9\Delta x^2} + b_2 \frac{f_{i+2} - 2f_i + f_{i-2}}{4\Delta x^2} + a_2 \frac{f_{i+1} - 2f_i + f_{i-1}}{\Delta x^2}, \quad (25)$$

where $\alpha_1 = 0.4442052$, $\beta_1 = 0.0383252$, $a_1 = 0.3855625$, $b_1 = 1.4861949$, and $c_1 = 0.0933036$. The resulting matrix equation is in the form, $Ax = b$, where A is a pentadiagonal matrix with $[\beta\alpha 1\alpha\beta]$. Hence a standard pentadiagonal solver [5] can be used to solve the system of equations.

The convective terms are solved in conservative form, except for the momentum equation, which is written in 'skew-symmetric' form

$$\frac{\partial(\rho u_k u_j)}{\partial x_j}\bigg|_i = \frac{1}{2} \left(\frac{\partial(\rho u_k u_j)}{\partial x_j} + \rho u_k \frac{\partial u_j}{\partial x_j} + u_j \frac{\partial \rho u_k}{\partial x_j} \right)_i. \quad (26)$$

Following [6], artificial diffusion is provided through artificial shear and bulk viscosity, μ^* and β^* , and thermal conductivity, k^* , as defined:

$$\mu^* = C_\mu \rho \Delta x^{r+2} |\nabla^r S|, \quad \beta^* = C_\beta \rho \Delta x^{r+2} |\nabla^r S|, \quad k^* = C_k \Delta x^{r+1} \frac{\rho a_0}{T} |\nabla^r e|, \quad (27)$$

where $r = 4$, $C_\mu^4 = 0.002$, $C_\beta^4 = 1$, $C_k = 0.01$, and a_0 is the reference sound speed. These artificial properties are added to the physical viscosities and thermal conductivities. Hence, even in inviscid calculations the diffusive terms must be com-

puted. The bi-harmonic operator is evaluated by applying the second derivatives twice. The overbar denotes a Gaussian filter,

$$\bar{f}_i = \frac{3565}{10,368} f_i + \frac{3091}{12,960} (f_{i-1} + f_{i+1}) + \frac{1997}{25,920} (f_{i-2} + f_{i+2}) + \frac{149}{12,960} (f_{i-3} + f_{i+3}) + \frac{107}{103,680} (f_{i-4} + f_{i+4}). \quad (28)$$

The diffusive terms are solved in the conservative form of Eq. (1) for the terms with artificial diffusivities and in non-conservative form

$$\frac{\partial \tau_{ij}}{\partial x_j} = \mu \frac{\partial^2 u_i}{\partial x_j^2} + \frac{\mu}{3} \frac{\partial \theta}{\partial x_i}, \quad \frac{\partial (u_i \tau_{ij})}{\partial x_j} = \tau_{ij} \frac{\partial u_i}{\partial x_j} + u_i \frac{\partial \tau_{ij}}{\partial x_j}, \quad \frac{\partial q_i}{\partial x_i} = -\frac{c_p \mu}{Pr} \frac{\partial^2 T}{\partial x_j^2}, \quad (29)$$

where $Pr = c_p \mu / k$, for the terms with physical diffusivities.

The time marching is handled using a two-step eleven-stage fourth-order accurate Runge–Kutta scheme optimized for low dispersion errors [19,43]; though more costly per time step, this time-marching scheme allows for larger time steps than the standard scheme. As in [6], the conserved variables are filtered after every Runge–Kutta substep using the following eighth-order accurate compact filter:

$$\beta \hat{f}_{i-2} + \alpha \hat{f}_{i-1} + \hat{f}_i + \alpha \hat{f}_{i+1} + \beta \hat{f}_{i+2} = \frac{e}{2} (f_{i+4} - f_{i-4}) + \frac{d}{2} (f_{i+3} - f_{i-3}) + \frac{c}{2} (f_{i+2} - f_{i-2}) + \frac{b}{2} (f_{i+1} - f_{i-1}) + a f_i, \quad (30)$$

where \hat{f} is the filtered variable, $\alpha = 0.66624$, $\beta = 0.16688$, $a = 0.99965$, $b/2 = 0.6665$, $c/2 = 0.16674$, $d/2 = 4 \times 10^{-5}$, and $e/2 = 5 \times 10^{-6}$.

B.2. The Stan-I code

In the improved *Stan-I* code, C_β is constructed such that artificial bulk viscosity is localized at shocks [3]:

$$C_\beta = \frac{1}{2} \left[1 - \tanh \left(2.5 + 10 \frac{\Delta}{a_0} \theta \right) \right] \frac{\theta^2}{\theta^2 + \omega_j \omega_j + \epsilon}. \quad (31)$$

B.3. The WENO code

For the *WENO* and *Hybrid* codes, the right-hand side of Eq. (23) is written as a flux difference $-(f_{i+1/2} - f_{i-1/2})/\Delta x$. In the *WENO* method, the Roe flux with entropy and carbuncle fixes are used; for simplicity, the procedure for the positive Roe flux is considered [21]. The fifth-order accurate procedure (used in the *Hybrid* code) is described. The relevant coefficients for the seventh-order accurate procedure can be found in the literature e.g., in Ref. [33]. The eigenvalues and eigenvector matrices $L_{i+1/2}$ and $R_{i+1/2}$ are computed using Roe averages. Then, the fluxes are projected into characteristic space to $g_j = L_{i+1/2} f_j$, $j \in [i-2, \dots, i+2]$. The flux at $x_{i+1/2}$ is given by

$$g_{i+1/2}^+ = \sum_{k=0}^2 \omega_{i+1/2}^{(k)} p_{i+1/2}^{(k)}, \quad (32)$$

where the plus sign represents a positive flux and

$$p_{i+1/2}^{(k)} = \sum_{l=0}^2 c_{rl} p_{i+1-l}^{(k)}, \quad \omega_{i+1/2}^{(k)} = \frac{\alpha_{i+1/2}^{(k)}}{\sum_{l=0}^2 \alpha_{i+1/2}^{(l)}}, \quad \alpha_{i+1/2}^{(k)} = \frac{d^{(k)}}{(\beta_{i+1/2}^{(k)} + \epsilon)^2}. \quad (33)$$

The $d^{(k)}$ and c_{rl} coefficients can be found in Ref. [40] and the smoothness indicators are given by

$$\begin{aligned} \beta_{i+1/2}^{(0)} &= \frac{13}{12} (g_{i+2} - 2g_{i+1} + 3g_i)^2 + \frac{1}{4} (g_{i+2} - 4g_{i+1} + g_i)^2, \\ \beta_{i+1/2}^{(1)} &= \frac{13}{12} (g_{i+1} - 2g_i + g_{i-1})^2 + \frac{1}{4} (g_{i+1} - g_{i-1})^2, \\ \beta_{i+1/2}^{(2)} &= \frac{13}{12} (g_i - 2g_{i-1} + g_{i-2})^2 + \frac{1}{4} (3g_i - 4g_{i-1} + g_{i-2})^2. \end{aligned} \quad (34)$$

The procedure is similar for the negative flux. Then, for each flux component, the sign of the eigenvalue specifies which flux is applied: if the eigenvalue is positive, the positive flux component is chosen; otherwise, the negative flux component is selected. The resulting numerical flux in characteristic space, $g_{i+1/2}$, is then projected back to real space: $f_{i+1/2} = R_{i+1/2} g_{i+1/2}$.

The diffusive terms are solved in non-conservative form using sixth-order accurate central differences, and the time-marching is handled using a standard four-stage fourth-order accurate Runge–Kutta scheme.

B.4. The Hybrid code

The numerical flux in the *Hybrid* code consists of the linear combination of a non-dissipative central term and a shock-capturing term:

$$f_{i+1/2} = f_{i+1/2}^{(c)} + \chi_{i+1/2} (f_{i+1/2}^{(w)} - f_{i+1/2}^{(c)}), \quad (35)$$

where the c and w superscripts denote central and WENO, respectively. The calculation of the WENO flux is described in the previous section.

The central fluxes are computed by an interpolation that, after applying $-(f_{i+1/2} - f_{i-1/2})/\Delta x$, is equivalent to the split form (given here for the mass flux)

$$\left. \frac{\partial(\rho u_j)}{\partial x_j} \right|_i = \frac{1}{2} \left(\frac{\partial(\rho u_j)}{\partial x_j} + \rho \frac{\partial u_j}{\partial x_j} + u_j \frac{\partial \rho}{\partial x_j} \right)_i. \quad (36)$$

The switching function is based on a dilatation/vorticity sensor similar to that of Ducros et al. [11]:

$$\chi = \frac{-\theta}{|\theta| + \sqrt{\omega_j \omega_j} + \epsilon}. \quad (37)$$

If $\chi > 0.65$, then χ is set to one; otherwise it is set to zero. This is done for neighboring points to ensure that central differencing is not done across any shocks.

The diffusive terms are solved in non-conservative form using sixth-order accurate central differences, and the time-marching is handled using a standard four-stage fourth-order accurate Runge–Kutta scheme.

B.5. The ADPDIS3D code

The high-order accurate filter method in *ADPDIS3D* consists of two steps, a full time step of the fourth-order Runge–Kutta base scheme step and a post-processing nonlinear filter step. For viscous gas dynamics, the same order of spatial centered base scheme for the convection terms and the viscous terms are employed. For all of the test cases, e.g., the spatial base scheme to approximate the inviscid flux derivatives $f(q)_x$ (with the grid indices k and l for the y - and z -directions suppressed) is written as

$$\frac{\partial f}{\partial x} \approx D_{08} f_j, \quad (38)$$

where D_{08} is the standard eighth-order accurate centered difference operator. After the completion of a full time step of the base scheme step, the second step is to adaptively filter the solution by the product of a wavelet sensor and the nonlinear dissipative portion of a high-resolution shock-capturing scheme. It can be obtained e.g., in the x -direction by taking the full seventh-order WENO scheme in the x -direction and subtracting $D_{08} f_j$. The final update of the solution is (with the filter numerical fluxes for the y - and z -direction suppressed)

$$q_{j,k,l}^{n+1} = q_{j,k,l}^* - \frac{\Delta t}{\Delta x} [H_{j+1/2} - H_{j-1/2}] \quad (39)$$

The nonlinear filter numerical fluxes usually involve the used of field-by-field approximate Riemann solvers. If Roe's type of approximate Riemann solver is employed, for example, the x -filter numerical flux vector $H_{j+1/2}$ is $H_{j+1/2} = R_{j+1/2} \bar{H}_{j+1/2}$, where $R_{j+1/2}$ is the matrix of right eigenvectors of the Jacobian of the inviscid flux vector in terms of the q^* solution from the base scheme step. Denote the elements of the vector $\bar{H}_{j+1/2}$ by $\bar{h}_{j+1/2}^l$, $l = 1, 2, \dots, 5$. The nonlinear portion of the filter $\bar{h}_{j+1/2}^l$ has the form

$$\bar{h}_{j+1/2}^l = \frac{1}{2} (s^N)_{j+1/2}^l (\phi_{j+1/2}^l). \quad (40)$$

Here $(s^N)_{j+1/2}^l$ is the wavelet flow sensor to activate the nonlinear numerical dissipation $\phi_{j+1/2}^l$. The dissipative portion of the nonlinear filter $\phi_{j+1/2}^l = g_{j+1/2}^l - b_{j+1/2}^l$ is the dissipative portion of the seventh-order WENO scheme for the local l th-characteristic wave. Here $g_{j+1/2}^l$ and $b_{j+1/2}^l$ are numerical fluxes of the seventh-order WENO scheme and the eighth-order central scheme for the l th characteristic, respectively. For all of the computations, a three-level second-order Harten multiresolution wavelet decomposition of the computed density and pressure is used as the flow sensor.

A summary of the three basic steps for obtaining the wavelet flow sensors is given in [41]. The computer routines to compute the wavelet coefficient of the second-order B-spline and the redundant form of Harten's multiresolution wavelets and their corresponding Lipschitz exponents of a given grid function f_j (e.g., density or pressure, or characteristic variables) can be found in the Appendix of Ref. [50].

Appendix C. Artificial diffusivity methods

In recent years, several artificial diffusivity methods have been proposed for calculations of compressible turbulence. The purpose of this section is to clarify the contribution and present the improvements of selected models.

To stabilize calculations of compressible isotropic turbulence, Shebalin [38] added a bulk viscosity that was constant in space. Cook and Cabot [7,8] improved on this idea by introducing Laplacian operators that attempt to localize the artificial bulk viscosity to shocks only, and by also introducing an artificial shear viscosity (intended to mimic a subgrid model) to damp near grid-scale vortical motions:

$$\mu^* = C_\mu \rho \Delta^{r+2} |\nabla^r \bar{S}|, \quad \beta^* = C_\beta \rho \Delta^{r+2} |\nabla^r \bar{S}|, \quad (41)$$

where $r = 4$, $C_\mu^4 = 0.002$, $C_\beta^4 = 1$, $\Delta = (\Delta x \Delta y \Delta z)^{1/3}$, and the bar denotes a truncated Gaussian filter. To be able to deal with contact discontinuities, Fiorina and Lele [13] proposed to, in addition, add artificial mass diffusivity to the continuity equation:

$$\chi^* = C_\rho \frac{a_0}{c_p} \Delta^{r+1} |\nabla^{r-1} \nabla s|, \quad (42)$$

where a_0 is the reference sound speed, c_p is the specific heat at constant pressure, s is the entropy, $r = 4$ and $C_\rho = 0.01$. Instead of including artificial mass diffusivity, Cook [6] proposed to add artificial thermal conductivity to capture contact discontinuities:

$$k^* = C_k \Delta^{r+1} \frac{\rho a_0}{T} |\nabla^r e|, \quad (43)$$

where e is the internal energy, $r = 4$ and $C_k = 0.01$. Kawai and Lele [22] later generalized the formulation of Cook [6] to curvilinear and anisotropic meshes, and modified the scaling of the artificial mass diffusivity in the species transport equations to better control under/overshoots in species concentration.

The results from the present collaborative effort have indicated that the artificial diffusivity method of Ref. [6] and that of Ref. [13] (data not shown) provides excessive damping of dilatational motions in compressible isotropic turbulence; this behavior was also noted in Ref. [9] in preliminary findings from the present study. This prompted Mani et al. [32] to re-define the artificial bulk viscosity to be a function of the dilatation rather than the strain-rate magnitude, since the latter includes vortical effects while shock waves do not:

$$\beta^* = C \Delta^{r+2} \rho |\nabla^r \theta| H(-\theta), \quad (44)$$

H is the Heaviside function that acts as a switch. Mani et al. [32] found that the sensitivity to the constant r is weak. The constant C may be different depending on the numerical scheme; values of $C = 1.0$ and $r = 4$ are used in Ref. [32]. In addition, a different implementation on curvilinear grids that removes the dependence on the grid spacing tangential to the shock is proposed.

Based on the insight of Mani et al. [32] that shock waves are associated only with the dilatational velocity field, Bhagatwala and Lele [3] later proposed a modified coefficient that activates the artificial bulk viscosity only in regions where the compression is strong compared to the vortical motions:

$$\beta^* = C_\beta \Delta^{r+2} \rho |\nabla^r \bar{S}|, \quad \text{where} \quad C_\beta = \frac{1}{2} \left[1 - \tanh \left(2.5 + 10 \frac{\Delta}{a_0} \theta \right) \right] \frac{\theta^2}{\theta^2 + \omega_j \omega_j + \epsilon}, \quad (45)$$

where the Ducros-type switch is used to sensitize β^* to the dilatation, and the hyperbolic tangent is used to “turn off” the bulk viscosity in regions of weakly compressive motions. Finally, Kawai et al. [23] used

$$\beta^* = C \Delta^{r+2} \rho |\nabla^r \theta| H(-\theta) \frac{\theta^2}{\theta^2 + \omega_j \omega_j + \epsilon}, \quad (46)$$

and applied the method to compressible isotropic turbulence and a turbulent boundary layer. They also showed that the coefficient $C = 1.75$ gives better results with the dilatation-based artificial bulk viscosity.

The key improvement of Mani et al. [32] over the method of Cook [6] stems from the realization that dilatation and the magnitude of the strain-rate tensor are similar at a shock, but that the former is orders of magnitude smaller in turbulence. The implications are twofold. First, dilatation is the variable on which the bulk viscosity is based; thus, the artificial bulk viscosity is activated only in regions in which dilatational changes are large. Second, the Heaviside function ensures that the coefficient is activated in regions of negative dilatation (compression). The application of the Laplacians serves two purposes: it determines the locations in which the artificial bulk viscosity must be applied and it regulates the magnitude of the coefficient. Hence, basing the artificial bulk viscosity on (negative) dilatation ensures that it is applied only in regions of large changes in compression. To highlight these improvements, Fig. 16 plots the dilatation spectrum for the compressible isotropic turbulence problem considered in Section 3.5 for the models of Mani et al. [32], Bhagatwala and Lele [3], and Kawai et al. [23], in addition to the original method of Cook [6]; the same underlying numerics are used (i.e., as described in Appendix B), but the model for the artificial bulk viscosity is based on the relevant reference. As expected from the results shown in

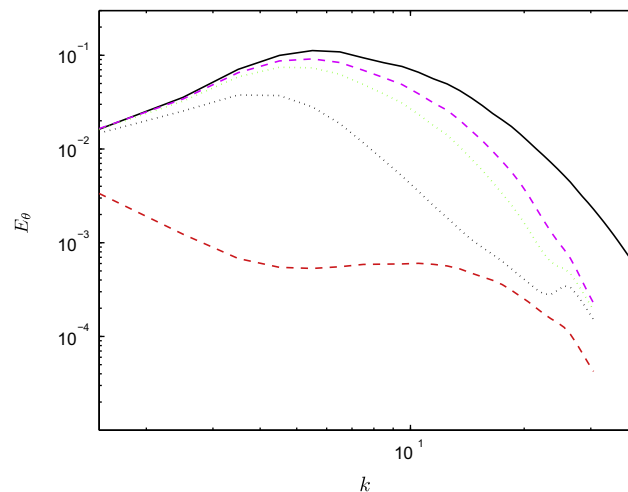


Fig. 16. Dilatation spectrum at $t/\tau = 4$ for the isotropic turbulence problem on a 64^3 grid for different artificial diffusivity methods. Red dash: [6]; black dash-dot: [32]; green dot: [23]; magenta dash (thin): [3]. (For interpretation of the references to colour in this figure legend, the reader is referred to the web version of this article.)

Section 3.5, the dilatation-based artificial bulk viscosity methods show significant improvement over the original method of [6] for a large range of wavenumbers. The implications of employing a Ducros-type switch in artificial diffusivity methods is not included here, as a detailed discussion on the use of different switching functions is provided in Ref. [23].

References

- [1] N.A. Adams, K. Shariff, A high-resolution hybrid compact-ENO scheme for shock-turbulence interaction problems, *J. Comput. Phys.* 127 (1996) 27–51.
- [2] M. Arora, P.L. Roe, On postshock oscillations due to shock-capturing schemes in unsteady flows, *J. Comput. Phys.* 130 (1997) 25–40.
- [3] A.V. Bhagatwala, S.K. Lele, A modified artificial nonlinear viscosity approach for compressible turbulence simulations, *J. Comput. Phys.* 228 (2009) 4965–4969.
- [4] M.E. Brachet, D.I. Meiron, S.A. Orszag, B.G. Nickel, R.H. Morf, U. Frisch, Small-scale structure of the Taylor–Green vortex, *J. Fluid Mech.* 130 (1983) 411–452.
- [5] W. Cheney, D. Kincaid, *Numerical Mathematics and Computing*, 4th ed., Brooks/Cole Thomson Learning, Belmont, CA, 2004.
- [6] A.W. Cook, Artificial properties for large-eddy simulation of compressible turbulent mixing, *Phys. Fluids* 19 (2007) 055103.
- [7] A.W. Cook, W.H. Cabot, A high-wavenumber viscosity for high-resolution numerical methods, *J. Comput. Phys.* 195 (2004) 594–601.
- [8] A.W. Cook, W.H. Cabot, Hyperviscosity for shock-turbulence interactions, *J. Comput. Phys.* 203 (2005) 379–385.
- [9] A.W. Cook, J. Larsson, W.H. Cabot, S.K. Lele, Simulation strategies for shock-turbulence interactions, in: *Proceedings of the Seventh International Symposium on Engineering Turbulence Modelling and Measurements*, European Research Collaboration on Flow Turbulence and Combustion, Limassol, Cyprus, 2008.
- [10] X. Deng, H. Zhang, Developing high-order weighted compact nonlinear schemes, *J. Comput. Phys.* 203 (2005) 22–44.
- [11] F. Ducros, V. Ferrand, F. Nicoud, C. Weber, D. Darracq, C. Gacherieu, T. Poinot, Large-eddy simulation of the shock/turbulence interaction, *J. Comput. Phys.* 152 (1999) 517–549.
- [12] F. Ducros, F. Laporte, T. Souleres, V. Guinot, P. Moinat, B. Caruelle, High-order fluxes for conservative skew-symmetric-like schemes in structured meshes: application to compressible flows, *J. Comput. Phys.* 161 (2000) 114–139.
- [13] B. Fiorina, S.K. Lele, An artificial nonlinear diffusivity method for supersonic reacting flows with shocks, *J. Comput. Phys.* 222 (2007) 246–264.
- [14] D.V. Gaitonde, M.R. Visbal, High-order Schemes for Navier–Stokes Equations: Algorithm and Implementation into FDL3DI, Technical Report AFRL-TR-98, US Air Force Research Lab, 1998.
- [15] E. Garnier, M. Mossi, P. Sagaut, P. Comte, M. Deville, On the use of shock-capturing schemes for large-eddy simulations, *J. Comput. Phys.* 153 (1999) 273–311.
- [16] J.A. Greenough, W.J. Rider, A quantitative comparison of numerical methods for the compressible Euler equations: fifth-order WENO and piecewise-linear Godunov, *J. Comput. Phys.* 196 (2004) 259–281.
- [17] M. Hahn, D. Drikakis, Large eddy simulation of compressible turbulence using high-resolution methods, *Int. J. Numer. Meth. Fluids* 47 (2005) 971–977.
- [18] D.J. Hill, D.I. Pullin, Hybrid tuned center-difference-WENO method for large eddy simulations in the presence of strong shocks, *J. Comput. Phys.* 194 (2004) 435–450.
- [19] F.Q. Hu, M.Y. Hussaini, J.L. Manthey, Low-dissipation and low-dispersion Runge–Kutta schemes for computational acoustics, *J. Comput. Phys.* 124 (1996) 177–191.
- [20] A. Jameson, W. Schmidt, E. Turkel, Numerical simulation of the Euler equations by finite volume methods using Runge–Kutta time stepping schemes, in: *Proceedings of the AIAA Fifth Computations Fluid Dynamics Conference*, 1981.
- [21] G.S. Jiang, C.W. Shu, Efficient implementation of weighted ENO schemes, *J. Comput. Phys.* 126 (1996) 202–228.
- [22] S. Kawai, S.K. Lele, Localized artificial diffusivity scheme for discontinuity capturing on curvilinear meshes, *J. Comput. Phys.* 227 (2008) 9498–9526.
- [23] S. Kawai, S.K. Shankar, S.K. Lele, Assessment of localized artificial diffusivity scheme for large-eddy simulation of compressible turbulent flows, *J. Comput. Phys.*, submitted for publication.
- [24] B. Kosovic, D.I. Pullin, R. Samtaney, Subgrid-scale modeling for large-eddy simulations of compressible turbulence, *Phys. Fluids* 14 (2002) 1511–1522.
- [25] J. Larsson, B. Gustafsson, Stability criteria for hybrid difference methods, *J. Comput. Phys.* 227 (2008) 2886–2898.
- [26] J. Larsson, S.K. Lele, P. Moin, Effect of Numerical Dissipation on the Predicted Spectra for Compressible Turbulence, Technical Report Ann. Res. Briefs, Center for Turbulence Research, Stanford University, 2007.
- [27] S. Lee, S.K. Lele, P. Moin, Eddy shocklets in decaying compressible turbulence, *Phys. Fluids* 3 (1991) 657–664.
- [28] R.J. LeVeque, *Finite Volume Methods for Hyperbolic Problems*, Cambridge University Press, Cambridge, UK, 2002.

- [29] R. Liska, B. Wendroff, Comparison of several difference schemes on 1D and 2D test problems for the Euler equations, *SIAM J. Sci. Comput.* 25 (2003) 995–1017.
- [30] C. Lui, S.K. Lele, Direct Numerical Simulation of Spatially Developing, Compressible, Turbulent Mixing Layers, AIAA-2001-0291, 2001.
- [31] K. Mahesh, The Interaction of a Shock Wave with a Turbulent Shear Flow, Ph.D. Thesis, Stanford University, 2000.
- [32] A. Mani, J. Larsson, P. Moin, Suitability of bulk viscosity for large-eddy simulation of turbulent flows with shocks, *J. Comput. Phys.* 228 (2009) 7368–7374.
- [33] M.P. Martin, E.M. Taylor, M. Wu, V.G. Weirs, A bandwidth-optimized WENO scheme for the effective direct numerical simulation of compressible turbulence, *J. Comput. Phys.* 220 (2006) 270–289.
- [34] W.F. Noh, Errors for calculations of strong shocks using an artificial viscosity and an artificial heat flux, *J. Comput. Phys.* 72 (1978) 78–120.
- [35] S. Pirozzoli, Conservative hybrid compact-WENO schemes for shock-turbulence interaction, *J. Comput. Phys.* 178 (2002) 81–117.
- [36] J.R. Ristorcelli, G.A. Blaisdell, Consistent initial conditions for the DNS of compressible turbulence, *Phys. Fluids* 9 (1997) 4–6.
- [37] R. Sanders, E. Morano, M.C. Druguet, Multidimensional dissipation for upwind schemes: stability and applications to gas dynamics, *J. Comput. Phys.* 145 (1998) 511–537.
- [38] J.V. Shebalin, Pseudospectral Simulation of Compressible Turbulence Using Logarithmic Variables, AIAA-93-3375-CP, 1993.
- [39] C.W. Shu, S. Osher, Efficient implementation of essentially non-oscillatory shock-capturing schemes II, *J. Comput. Phys.* 93 (1989) 32–78.
- [40] C.W. Shu, Essentially Non-oscillatory and Weighted Essentially Non-oscillatory Schemes for Hyperbolic Conservation Laws, ICASE Report No. 97-65, NASA Langley Research Center, 1997.
- [41] B. Sjögreen, H.C. Yee, Multiresolution wavelet-based adaptive numerical dissipation control for high-order methods, *J. Sci. Comput.* 20 (2004) 211–255.
- [42] B. Sjögreen, H.C. Yee, On skew-symmetric splitting and entropy conservation schemes for the Euler equations, in: *Proceedings of the Eighth European Conference on Numerical Mathematics and Advanced Applications*, Uppsala, Sweden, submitted for publication.
- [43] D. Stanescu, W.G. Habashi, 2N-storage low dissipation and dispersion Runge–Kutta schemes for computational acoustics, *J. Comput. Phys.* 143 (1998) 674–681.
- [44] G.I. Taylor, A.E. Green, Mechanism of the production of small eddies from large ones, *Proc. R. Soc. London A* 158 (1937) 499–521.
- [45] E.F. Toro, *Riemann Solvers and Numerical Methods for Fluid Dynamics*, Springer-Verlag, Heidelberg, Germany, 1999.
- [46] M.R. Visbal, D.V. Gaitonde, Shock Capturing Using Compact-differencing-based Methods, AIAA-2005-1265, 2005.
- [47] P. Woodward, P. Colella, The numerical simulation of two-dimensional fluid flow with strong shocks, *J. Comput. Phys.* 54 (1984) 115–173.
- [48] H.C. Yee, N.D. Sandham, M.J. Djomehri, Low-dissipative high-order shock-capturing methods using characteristic-based filters, *J. Comput. Phys.* 150 (1999) 199–238.
- [49] H.C. Yee, M. Vinokur, M.J. Djomehri, Entropy splitting and numerical dissipation, *J. Comput. Phys.* 162 (2000) 33–81.
- [50] H.C. Yee, B. Sjögreen, Development of low dissipative high-order filter schemes for multiscale Navier–Stokes/MHD systems, *J. Comput. Phys.* 225 (2007) 910–934.
- [51] H.C. Yee, B. Sjögreen, Adaptive filtering and limiting in compact high-order methods for multiscale gas dynamics and MHD systems, *Comput. Fluids* 37 (2008) 593–619.
- [52] X. Zhong, High-order finite-difference schemes for numerical simulation of hypersonic boundary-layer transition, *J. Comput. Phys.* 144 (1998) 662–709.